

# Evidence for polycyclic aromatic hydrocarbons detected in sulfates at Jezero crater by the Perseverance rover

Teresa Fornaro<sup>1\*</sup>, Sunanda Sharma<sup>2,3</sup>, Ryan S. Jakubek<sup>4</sup>, Giovanni Poggiali<sup>1</sup>, John Robert Brucato<sup>1</sup>, Rohit Bhartia<sup>5</sup>, Andrew Steele<sup>3</sup>, Ashley E. Murphy<sup>6</sup>, Mike Tice<sup>7</sup>, Mitchell D. Schulte<sup>8</sup>, Kevin P. Hand<sup>2</sup>, Marc D. Fries<sup>9</sup>, William J. Abbey<sup>2</sup>, Andrew Alberini<sup>1,10</sup>, Daniela Alvarado-Jiménez<sup>11,12</sup>, Kathleen C. Benison<sup>13</sup>, Eve L. Berger<sup>9</sup>, Sole Biancalani<sup>1,14,15,16</sup>, Adrian J. Brown<sup>17</sup>, Adrian Broz<sup>18</sup>, Wayne P. Buckley<sup>4</sup>, Denise K. Buckner<sup>19,20</sup>, Aaron S. Burton<sup>21</sup>, Sergei V. Bykov<sup>22</sup>, Emily L. Cardarelli<sup>23</sup>, Edward Cloutis<sup>24</sup>, Stephanie A. Connell<sup>25</sup>, Cristina Garcia-Florentino<sup>1</sup>, Felipe Gómez<sup>26</sup>, Nikole C. Haney<sup>4,27,28</sup>, Carina Lee<sup>4,27,28</sup>, Valeria Lino<sup>11</sup>, Paola Manini<sup>29</sup>, Francis M. McCubbin<sup>9</sup>, Michelle Minitti<sup>30</sup>, Richard V. Morris<sup>9</sup>, Yu Yu Phua<sup>31</sup>, Nicolas Randazzo<sup>32</sup>, Joseph Razzell Hollis<sup>33</sup>, Francesco Renzi<sup>1,34</sup>, Sandra Siljeström<sup>35</sup>, Justin I. Simon<sup>9</sup>, Anushree Srivastava<sup>3</sup>, Nicola Tasinato<sup>11</sup>, Kyle Uckert<sup>2</sup>, Roger C. Wiens<sup>25</sup>, Amy J. Williams<sup>36</sup>

<sup>1</sup>INAF-Astrophysical Observatory of Arcetri, Florence, Italy

<sup>2</sup>Jet Propulsion Laboratory, California Institute of Technology, Pasadena, USA

<sup>3</sup>Carnegie Science Earth & Planets Laboratory, Washington, DC, USA

<sup>4</sup>Amentum JETS II, NASA Johnson Space Center, Houston, TX, USA

<sup>5</sup>Photon Systems Incorporated, Covina, CA, USA

<sup>6</sup>Planetary Science Institute, Tucson, AZ, USA

<sup>7</sup>Department of Geology and Geophysics, Texas A&M University, College Station, TX, USA

<sup>8</sup>Mars Exploration Program, NASA Headquarters, Washington, DC, USA

<sup>9</sup>Astromaterials Research and Exploration Science Division, NASA Johnson Space Center, Houston, TX, USA

<sup>10</sup>Department of Physics and Astronomy, University of Florence, Sesto Fiorentino, Florence, Italy

<sup>11</sup>Scuola Normale Superiore di Pisa, Pisa, Italy

<sup>12</sup>IUSS, Scuola Universitaria Superiore Pavia, Pavia, Italy

<sup>13</sup>Department of Geology and Geography, West Virginia University, Morgantown, WV, USA

<sup>14</sup>Department of Physics, University of Trento, Povo, Italy

<sup>15</sup>Italian Space Agency (ASI), Rome, Italy

<sup>16</sup>Department of Earth Sciences, University of Florence, Florence, Italy

<sup>17</sup>Plancus Research, Severna Park, MD, USA

<sup>18</sup>Department of Earth Sciences, University of Oregon Eugene, Oregon, USA

<sup>19</sup>NASA Goddard Space Flight Center, Greenbelt, MD, USA

<sup>20</sup>Oak Ridge Associated Universities, Oak Ridge, TN, USA

<sup>21</sup>Planetary Science Division, NASA Headquarters, Washington, DC, USA

<sup>22</sup>Department of Chemistry, University of Pittsburgh, Pittsburgh, PA, USA

<sup>23</sup>Department of Earth, Planetary and Space Sciences, University of California, Los Angeles

<sup>24</sup>Centre for Terrestrial and Planetary Exploration, University of Winnipeg, Winnipeg, Manitoba, Canada

<sup>25</sup>Earth, Atmospheric, and Planetary Sciences, Purdue University, West Lafayette, IN, USA

<sup>26</sup>Centro de Astrobiología (CAB), CSIC-INTA, Torrejón de Ardoz, Spain

<sup>27</sup>Texas State University, Houston, TX, USA

<sup>28</sup>NASA Johnson Space Center, Houston, TX, USA

<sup>29</sup>Department of Chemical Sciences, University of Naples Federico II, Naples, Italy

<sup>30</sup>Framework, Silver Spring, MD, USA

<sup>31</sup>Division of Geological and Planetary Sciences, California Institute of Technology, Pasadena, CA, USA

<sup>32</sup>University of Alberta, Department of Earth and Atmospheric Sciences, Edmonton, Alberta, Canada

<sup>33</sup>Natural History Museum, London, UK

<sup>34</sup>University of Pisa, Pisa, Italy

<sup>35</sup>RISE Research Institutes of Sweden, Stockholm, Sweden

<sup>36</sup>Department of Geological Sciences, University of Florida, Gainesville, FL, USA

\*e-mail: [teresa.fornaro@inaf.it](mailto:teresa.fornaro@inaf.it)

**The search for organic molecules on Mars is central to understanding the planet’s past habitability and potential for ancient life. Although organics have been previously detected on Mars, their nature, origin, and preservation mechanisms remain debated. On the floor of the Jezero crater—an ancient delta-lake system on Mars—the *Perseverance* rover detected Raman features possibly due to organics spatially associated with sulfates, though their origin is uncertain. Here, we report the detection of similar Raman features in the Jezero fan top and attribute them to polycyclic aromatic hydrocarbons (PAHs) based on comparison with laboratory data. We propose that PAHs may have formed through endogenous igneous processes and were subsequently preserved by sulfate precipitation. These findings align with previous studies on Martian meteorites and at Gale crater, underscoring the role of sulfates in preserving organics on Mars. Returning these samples to Earth would be key to assess their astrobiological significance.**

An important objective of the NASA Mars 2020 mission is to collect astrobiologically relevant rocks to be returned to Earth through the planned NASA-ESA Mars Sample Return (MSR) Campaign<sup>1</sup>. Detection of organic matter is key to assess past habitability and identify potential biosignatures, as simple organic compounds can be nutrients for life and complex organic compounds can provide direct evidence of biogenicity. The Scanning Habitable Environments with Raman and Luminescence for Organics and Chemicals (SHERLOC) instrument onboard the Mars 2020 *Perseverance* rover, a deep UV (DUV) Raman and fluorescence spectrometer, detected intriguing spectral features in the Jezero crater floor, possibly consistent with aromatic organic compounds in association with sulfate minerals<sup>2</sup>. Specifically, Sharma et al.<sup>2</sup> reported Raman features in spectral regions of interest for organics, i.e., 1300-1500 cm<sup>-1</sup> and 1600-1700 cm<sup>-1</sup>,

associated with sulfates in the Quartier abrasion target (QRT) of the Issole outcrop, and co-located with a fluorescence doublet at ~303 and 325 nm. The Robine and Malay cores were taken from this outcrop, an olivine cumulate of the Jezero crater floor. The authors attributed the origin of these Raman features to either organic molecules or nitrates, and the fluorescence to aromatic organics or  $Ce^{3+}$  in anhydrite. Here, we report the detection of similar Raman features in association with sulfates observed in Pilot Mountain (PMT) and Dragon's Egg Rock (DER) targets in the Jezero fan top. PMT is a core collected from the Dream Lake outcrop, interpreted as a likely fluvial sandstone with grains sourced primarily from an olivine-rich area and a bulk composition broadly consistent with a mafic or ultramafic provenance modified by aqueous alteration<sup>3</sup>. Textural observations show the presence of pore-filling phases. SHERLOC analyzed its natural surface after dust removal on sol 874. DER is an abraded target on the Mount Meeker boulder, whose crystalline texture and bulk composition are consistent with an igneous or altered igneous rock<sup>4</sup>. It contains a sulfate vein analyzed by SHERLOC on sol 861. To expand on the organic hypothesis presented in Sharma et al.<sup>2</sup> and to provide potential organic candidates for the spectral features detected in the Jezero crater floor and fan, this work compares the SHERLOC results with laboratory data from reference organo-sulfate samples acquired using SHERLOC-analog instruments, and evaluates the possible organic sources.

### **SHERLOC observations**

We specifically searched for Raman features in the spectral regions relevant to organics in 839 SHERLOC spectra where Raman sulfate features with signal-to-noise ratio (SNR)  $> 5$  were identified by Sharma et al.<sup>2</sup>, Siljeström et al.<sup>5</sup>, and Phua et al.<sup>6</sup> in natural surfaces and abrasions investigated up to the fan top. The spectra included 42 from 4 targets among 11 analyzed in the crater floor, 529 from 5 targets among 11 analyzed in the fan front, and 268 from 6 targets among 10 analyzed in the fan top.

As reported by Sharma et al.<sup>2</sup>, in the crater floor, the QRT target has 1 spectrum acquired on sol 293 and 3 spectra acquired on sol 304 exhibiting Raman features in spectral regions relevant to organics, associated with sulfate Raman features. Fitting the average spectrum with Voigt functions, we identified peaks at:  $1340 \pm 4 \text{ cm}^{-1}$  with SNR 11 and full-width at half-maximum (FWHM)  $70 \pm 20 \text{ cm}^{-1}$ ;  $1395 \pm 2 \text{ cm}^{-1}$  with SNR 12 and FWHM  $39 \pm 5 \text{ cm}^{-1}$ ;  $1440 \pm 40 \text{ cm}^{-1}$  with SNR 7 and FWHM  $80 \pm 30 \text{ cm}^{-1}$ ; and  $1643.4 \pm 0.2 \text{ cm}^{-1}$  with SNR 7 and FWHM  $42 \pm 4 \text{ cm}^{-1}$  (Fig. 1). In addition, a shoulder around  $1255 \text{ cm}^{-1}$  on the tail of a band of magnesium sulfate suggests the presence of a peak that cannot be fitted.

In the fan top, we found 2 noisier spectra, measured on the natural surface of the PMT target after dust removal, whose average exhibits peaks at:  $1273 \pm 5 \text{ cm}^{-1}$  with SNR 5 and FWHM  $50 \pm 90 \text{ cm}^{-1}$ ;  $1360 \pm 90 \text{ cm}^{-1}$  with SNR 17 and FWHM  $60 \pm 200 \text{ cm}^{-1}$ ;  $1410 \pm 50 \text{ cm}^{-1}$  with SNR 20 and FWHM  $60 \pm 100 \text{ cm}^{-1}$ ;  $1480 \pm 20 \text{ cm}^{-1}$  with SNR 10 and FWHM  $50 \pm 100 \text{ cm}^{-1}$ ; and  $1646 \pm 7 \text{ cm}^{-1}$  with SNR 10 and FWHM  $70 \pm 40 \text{ cm}^{-1}$  (Fig. 2b). These Raman features are similar to QRT observations and are also co-located with a fluorescence doublet at ~303 and 325 nm (Fig. 2c).

In another fan top target, DER, we also found that the average spectrum acquired on a sulfate vein targeted on sol 861 exhibits peaks at:  $1338.813 \pm 0.002 \text{ cm}^{-1}$  with SNR 14 and FWHM  $45 \pm 3 \text{ cm}^{-1}$ ;  $1403.125 \pm 0.001 \text{ cm}^{-1}$

with SNR 14 and FWHM  $73.5 \pm 0.4 \text{ cm}^{-1}$ ; and  $1630.521 \pm 0.003 \text{ cm}^{-1}$  with SNR 15 and FWHM  $46 \pm 6 \text{ cm}^{-1}$  (Fig. 3b). The co-located fluorescence exhibits a weak band at 325-330 nm (Fig. 3c).

SHERLOC and PIXL data revealed magnesium and calcium sulfates as the dominant mineral phases co-located with the above spectral features<sup>5,6</sup> (see Identification of main mineral phases in Methods).

We did not detect Raman spectral features in ranges relevant to organics with SNR  $> 5$  among the 529 SHERLOC spectra exhibiting sulfate detection in any fan front targets.

### **Cross-comparison with laboratory analog data**

To assess whether organics associated with sulfates could produce DUV Raman spectral features as observed in these Jezero targets, we prepared organo-sulfate analog samples and characterized them with laboratory DUV Raman and fluorescence spectrometers analogous to SHERLOC (see Methods), looking for concomitant correlations between Raman organic spectral features and fluorescence spectral features. We used aromatic organic compounds of both abiotic and potential biotic origin, which are easily detectable with SHERLOC due to resonance enhancement, and hydrated magnesium sulfates as mineral substrates because we observed shifts in peak positions with respect to reference sulfate spectra for hydrated magnesium sulfates in QRT within  $20 \text{ cm}^{-1}$  (see Extended Data Fig. 1a), possibly indicative of molecule-mineral interactions<sup>7-10</sup>.

Comparison between our laboratory dataset and SHERLOC observations for QRT and PMT shows that different types of aromatic organics in sulfates tested in this work—naphthalene, 1- and 2-naphthol (HN), 1,3- and 2,6-dihydroxynaphthalene (DHN), 9-methylanthracene (9-MA), uracil and an oxy-PAH polymer synthesized from 1-HN (poly1-HN)—exhibit intense C-C and C=C ring stretching bands (and C=O stretching bands in the case of compounds like uracil with carbonyl functional groups on the aromatic ring)<sup>11</sup> at a variety of positions within the spectral regions of interest for QRT and PMT, though none of the tested organo-sulfate analogs exhibit fluorescence resembling the co-located fluorescence doublet at  $\sim 303$  and 325 nm observed in QRT and PMT (Fig. 4). Rather, the PAHs 9-MA, 2,6-DHN and 1,3-DHN in magnesium sulfate fluoresce mostly outside the SHERLOC region, which may be consistent with an inorganic hypothesis of the co-located fluorescence doublet, such as luminescence of  $\text{Ce}^{3+}$  in anhydrite<sup>12,13</sup> (see Inorganic interpretation of fluorescence observations in Methods), illustrating that similar types of three/two-ring aromatic organic molecules could be present.

In particular, 9-MA in magnesium sulfate has three main peaks in the spectral regions of interest, centered at 1618, 1402 and  $1251 \text{ cm}^{-1}$  (for detailed assignments of vibrational modes, see Computational spectroscopy simulations in Methods). The first two span the same spectral ranges of QRT and PMT main features of interest and exhibit the same peak height ratios (Table 1). The third one falls in a region of the QRT and PMT spectra where tails of sulfate bands hinder detection. In the case of PMT, however, we were able to tentatively fit a peak at  $1273 \text{ cm}^{-1}$  with FWHM of  $\sim 40 \text{ cm}^{-1}$  and peak height ratio with respect to the peak at  $1646 \text{ cm}^{-1}$  of 0.6, similar to the peak height ratio of 0.8 obtained for the peaks of 9-MA in magnesium sulfate at 1251 and  $1618 \text{ cm}^{-1}$ . All the other bands of 9-MA are weaker and would be more difficult for SHERLOC to detect.

2,6-DHN in magnesium sulfate displays peaks at 1610 and 1370  $\text{cm}^{-1}$ , which are shifted by -33 and -25  $\text{cm}^{-1}$  relative to the QRT features of interest, respectively, and their height ratio is half the QRT ones (Table 1); thus, it is unlikely that this PAH contributes to the QRT features of interest.

In contrast, a better match in terms of peak positions is observed for 1,3-DHN in magnesium sulfate, which exhibits two main Raman peaks centered at 1627 and 1391  $\text{cm}^{-1}$  (Table 1), while the peak height ratio between the peaks at 1391 and 1627  $\text{cm}^{-1}$  is half that observed for the corresponding QRT features of interest, meaning that the peak of 1,3-DHN in magnesium sulfate at 1391  $\text{cm}^{-1}$  might only partly contribute to the features of interest observed in QRT in that region. However, the presence of both 9-MA and 1,3-DHN would give an overall good agreement both in terms of peak positions and peak height ratios, indicating that a mixture of PAHs like 9-MA and 1,3-DHN in magnesium sulfate might explain the most prominent features observed by SHERLOC in QRT in the spectral regions relevant to organics. The spectral shifts observed for these molecules may be due to slight differences in molecular structure and/or the actual mineral matrix present in the martian samples, which is a mixture of multiple mineral phases, and the likely presence of multiple similar organics, as expected for natural samples. Importantly, the magnitude of these shifts is consistent with that observed for the main bands assigned to hydrated magnesium sulfates in QRT's points of interest with respect to reference magnesium sulfates, which may be caused by molecule-mineral interactions<sup>7-10</sup>. On the other hand, the invariance of the peak positions of the main features assigned to anhydrite in QRT suggests that the anhydrous calcium sulfates in QRT should not be involved in interactions with organic molecules. These observations would be consistent with the organics being incorporated into magnesium sulfates through aqueous processes, and anhydrite being formed at another stage through a separate process.

The main sulfates present in QRT points of interest that were previously identified by Siljeström et al.<sup>5</sup>, also exhibit minor Raman bands in the spectral regions of interest, as shown in the inset of Extended Data Fig. 1a, but they do not give a good match with QRT since the spectral shifts range from 40 to 100  $\text{cm}^{-1}$  and the peak heights are approximately two to thirteen times lower (Table 1). In the PMT points of interest, anhydrite with minor bassanite are the main sulfates, as previously identified by Phua et al.<sup>6</sup>. These phases exhibit minor peaks at 1357 and 1621  $\text{cm}^{-1}$ , which have heights about ten and five times lower than the PMT features of interest, respectively (Table 1). In DER, bassanite is the main sulfate in the light toned vein targeted by SHERLOC on sol 861 (see Identification of main mineral phases in Methods). This phase exhibits minor peaks at 1333 and 1619  $\text{cm}^{-1}$  with shifts within 12  $\text{cm}^{-1}$  and similar peak height ratios (Table 1). Given this spectral match, the most straightforward interpretation is that these minor bands of bassanite account for the Raman features of interest in DER, even though the features of 1,3-DHN in magnesium sulfate also show good agreement (Table 1). This interpretation is consistent with the widespread spatial distribution of these features throughout the targeted sulfate vein in DER. In contrast, the organic hypothesis for the Raman features of interest in QRT and PMT is consistent with their spatial distribution concentrated in a limited area of the targets.

## Potential mechanisms for the presence of PAHs in sulfates in Quartier and Pilot Mountain

To explain the presence of PAHs in sulfates in the QRT and PMT targets, four scenarios are presented in Fig. 5.

Scenario 1 hypothesizes an endogenous igneous organics formation. This is supported by the observation of the intriguing Raman features only in the aqueously altered olivine cumulate in the crater floor target of QRT and the olivine-rich fan top target of PMT, but not in the fan front where primary minerals have been commonly overprinted by secondary minerals. Scenario 1 points to better preservation when organics are intimately mixed with, or even included within, primary minerals. A similar association of organic carbon within magmatic minerals has been found in Martian meteorites<sup>14</sup>, suggesting that an abiotic reservoir of primary organic carbon formed through igneous processes could be nearly ubiquitous in Martian igneous rocks<sup>15-17</sup>. Furthermore, the location of these features of interest suggests accumulation of organics in mineral inclusions or pores of igneous rocks. This would be consistent with an abiotic synthesis from trapped magmatic gases or CO<sub>2</sub>, catalyzed by iron oxides from solid volcanic products<sup>18-21</sup>, which are present in QRT and possibly in PMT, and/or condensation on olivine walls during cooling of magmatic reduced fluids trapped as olivine-hosted inclusions<sup>14,22,23</sup>. Indeed, complex PAHs have been shown in the Martian meteorite ALH84001 to be associated with graphitic particles attached to magnetite grains<sup>17</sup>. The detection of methylated PAHs supports this scenario, as they are more stable than their parent compounds across the entire temperature range for hydrocarbon formation in aqueous processes or from volcanic gases<sup>19</sup>. Because QRT is an igneous rock, its observations could be compatible with *in situ* igneous formation of PAHs and subsequent preservation by sulfates<sup>24-26</sup> precipitated in the pores of the igneous rock as a consequence of aqueous alteration (Scenario 1A). An alternate explanation, Scenario 1B, would involve an *ex situ* igneous formation of PAHs, followed by fluid transport. Textural observations of PMT indicate it is a fan top sandstone that likely formed as a fluvial deposit. Its igneous lithic grains were sourced from an olivine-rich area, where PAHs may have formed through igneous processes. PAHs would have been subsequently mobilized by groundwater and co-precipitated with sulfates or trapped and preserved within sulfate cement crystals. This would be consistent with the spatial arrangement of the observed material primarily concentrated in one area, similar to organics concentrated as the sample dehydrates. Scenario 1B would also be consistent with QRT observations suggesting incorporation of organics into sulfates through aqueous processes. Moreover, the fluid transportation mechanism would be responsible for selective accumulation of PAHs in these rocks instead of macromolecular carbon (MMC). PAHs have a higher mobility in fluid phases and can be leached from rocks more easily than MMC when fluids flow through fractures due to their smaller molecular size and greater solubility, whereas MMC remains largely immobile and confined to its original location unless broken into smaller units.

Regional hydrothermal groundwaters associated with Syrtis Major volcanism might also have played a role in sulfate formation and PAH transportation<sup>27</sup> (Scenario 2), as well as in dissolving igneous rocks causing mobilization of Ce<sup>3+</sup> and its transportation through fractures and precipitation as sulfate veins, which would explain the co-presence of Ce<sup>3+</sup> and PAHs in these sulfates.

Exogenous delivery of PAHs or production during shock impact processes<sup>28</sup> (Scenario 3) is a scenario often considered in detections of organics in Martian meteorites because impact processes are necessarily linked to

their delivery mechanism to Earth. Although QRT and PMT are within an impact crater on Mars, this scenario seems unlikely due to the lack of evidence that these rocks were formed by impact processes from the Jezero crater impact<sup>29,30</sup>.

Finally, we also consider the hypothesis that the observed organic-sulfate relationship is a result of ancient microbial life or its residues participating in weathering reactions during the period in aqueous alteration/diagenesis when sulfates were formed (Scenario 4)<sup>31</sup>, although no preserved evidence exists in these rocks for such a mechanism.

Detailed analysis of the returned samples through a variety of other techniques will enable to distinguish between these different scenarios.

## Conclusions

SHERLOC detected complex Raman features in spectral ranges relevant to organics, i.e. 1300-1500 and 1600-1700  $\text{cm}^{-1}$ , in association with sulfates in the QRT target of the Jezero crater floor, and in the PMT and DER targets of the Jezero fan top. These observations were compared against laboratory studies using reference sulfates and organo-sulfate analogs. The outcomes of these laboratory investigations suggest that the Raman features of interest in DER are likely due to minor bands of bassanite, while the ones in QRT and PMT might have some organic contributions from a mixture of PAHs, like methylanthracenes and dihydroxynaphthalenes that do not produce fluorescence in the range detectable by SHERLOC, with the co-located fluorescence doublet at  $\sim 303$  and  $325$  nm likely caused by inorganic sources, such as luminescence of  $\text{Ce}^{3+}$  in anhydrite<sup>12,13</sup>. Other structurally similar PAHs not tested here may provide a similar match and help explain the multiple components of the broad feature observed in the spectral region 1300-1500  $\text{cm}^{-1}$ . Future dedicated work will also investigate other possible inorganic contributions to these multi-component Raman features of interest. The presence of these features in igneous rocks suggests an endogenous igneous formation process for PAHs in QRT and PMT, and their association with sulfates suggests salt-mediated preservation. Preservation by sulfates might have enabled the observation of an immature refractory organic material, still containing three- and two-ring aromatic PAH-like units, detectable down to sub-part per million levels due to resonance enhancement in DUV Raman. This work is consistent with studies on Martian meteorites<sup>32</sup> and observations from Gale crater<sup>33</sup> and reinforces the hypothesis that sulfates could be crucial in the preservation and transport of organic molecules in the Martian environment and, hence, could have played a significant role in the Martian carbon cycle, influencing the availability and cycling of carbon compounds necessary for life. Although we have not found evidence of biogenicity, we cannot completely rule out that the organics potentially detected in these rocks might be resistant alteration products from the chemical weathering of ancient biotic compounds. With the limitations of *Perseverance*'s Raman and fluorescence spectroscopy techniques—inherently less diagnostic than the mass spectrometry methods used by the *Curiosity* rover, which provides more definitive chemical identification—addressing these various hypotheses would require further laboratory studies to retrace the chemical weathering processes that might have occurred at Jezero crater over time leading to the

formation of the observed organics, and returning these samples to Earth for high sensitive analysis in Earth-based laboratories as part of the Mars Sample Return Campaign. *Perseverance* currently carries onboard the PMT core and the Robine core, with the latter collected from the same rock where the QRT abrasion was analyzed. Moreover, the twin core of Robine, named Malay, was placed on the surface of Mars in the first depot of samples at the Three Forks area in Jezero crater. In-depth analyses of these cores on Earth could reveal important details about the Martian carbon cycle, the habitability potential of the sites explored by *Perseverance* and the astrobiological relevance of these samples.

## Methods

**Identification of main mineral phases.** Siljeström et al.<sup>5</sup> identified anhydrite mixed with hydrated magnesium sulfate as main sulfates in QRT: the sulfate  $\nu_1$  and  $\nu_3$  peak positions match well with those of anhydrite, while the O-H bands at  $\sim 3200$  and  $\sim 3400$   $\text{cm}^{-1}$  are most likely from hydrated magnesium sulfate phases mixed with the anhydrite because they are not a good match for either gypsum or bassanite. PIXL co-located measurements confirmed the presence of calcium and magnesium sulfates<sup>5</sup>. In particular, hydrated magnesium sulfate phases with four water molecules (starkeyite) and one/two water molecules seem to be mainly present in the points of interest, as reported by Siljeström et al.<sup>5</sup> and shown in Extended Data Fig. 1a. Indeed, there is almost a perfect match of peak height ratios between the  $1061$   $\text{cm}^{-1}$  and  $3185$   $\text{cm}^{-1}$  peaks in QRT and the  $\nu_1$  at  $1041$   $\text{cm}^{-1}$  and  $\nu_{\text{OH}}$  at  $3201$   $\text{cm}^{-1}$  of magnesium sulfate mono/dihydrate, even though peak positions differ of  $-20$  and  $16$   $\text{cm}^{-1}$ , respectively. The minor peak at  $1210$   $\text{cm}^{-1}$  in QRT can be assigned to a magnesium sulfate mono/dihydrate peak at  $1212$   $\text{cm}^{-1}$ , which exhibits a similar peak height ratio with respect to  $\nu_1$ . The starkeyite  $\nu_1$  peak falls below the dominant anhydrite  $\nu_1$  peak, while the  $3399$   $\text{cm}^{-1}$  peak in QRT can be attributed to the starkeyite  $\nu_{\text{OH}}$  at  $3410$   $\text{cm}^{-1}$ , shifted by  $+11$   $\text{cm}^{-1}$ . The peak at  $952$   $\text{cm}^{-1}$  in QRT was assigned to perchlorate or phosphate by Corpolongo et al.<sup>34</sup>. Based on PIXL maps, there is no phosphate in the points of interest (Supplementary Fig. 1, top panel), while there is a small amount of chlorine (1-2%), which increases confidence that the  $952$   $\text{cm}^{-1}$  peak is likely due to perchlorate. In the case of PMT, according to PIXL maps (Supplementary Fig. 1, central panel), the main sulfates are calcium sulfates with minor magnesium and iron sulfates, and the interesting SHERLOC features are in the white patch composed mainly of calcium sulfate. The weak Raman hydration features detected by SHERLOC in the points of interest indicate that the calcium sulfate in PMT is slightly hydrated. A reference sample of anhydrite with minor bassanite matches the main sulfate bands and hydration features observed in PMT points of interest, as shown in Extended Data Fig. 1b. This agrees with assignments reported by Phua et al.<sup>6</sup>. In the case of DER, no co-located PIXL maps are available in the area scanned by SHERLOC in the detail 1 scan on sol 861. However, a PIXL map was acquired on another part of the same vein, which contains mainly calcium sulfate and magnesium-iron sulfates, as shown in Supplementary Fig. 1 (bottom panel). Based on comparison with DUV Raman spectra of reference calcium sulfates, bassanite can be identified as the main calcium sulfate in the vein targeted by SHERLOC in the detail

1 scan on sol 861, as shown in Extended Data Fig. 1c. Luminescence from  $\text{Ce}^{3+}$  in phosphates has been reported to occur in the range 330-350 nm<sup>35,36</sup>, similar to the fluorescence observed in DER when averaging all spectra of the detail 1 scan acquired on sol 861 (Fig. 3). However, no phosphate bands are observed in the corresponding SHERLOC Raman spectra, and the part of the vein intersected by the PIXL map presents minimal  $\text{P}_2\text{O}_5$  content (<0.3%), as shown in Supplementary Fig. 1 (bottom panel). Although, without co-located PIXL maps for the area scanned by SHERLOC, it remains unclear whether trace amounts of phosphate exist below SHERLOC's detection threshold, given that SHERLOC's sensitivity to  $\text{Ce}^{3+}$  in phosphate minerals far exceeds its sensitivity to the  $\nu_1$  phosphate band in Raman spectra<sup>36</sup>.

**Inorganic interpretation of fluorescence observations.** None of the tested organo-sulfate analogs exhibit fluorescence resembling the co-located fluorescence doublet at ~303 and 325 nm observed in QRT and PMT points of interest, while a very good match is observed with the DUV fluorescence spectrum of the anhydrite reference sample used in this work (Supplementary Fig. 2a), which contains  $794 \pm 9$  part per billion of cerium as measured by ICP-MS. This further corroborates the hypothesis that the fluorescence doublet has an inorganic origin, such as luminescence from  $\text{Ce}^{3+}$  substituted for Ca within anhydrite<sup>12,13</sup>. Moreover, subjecting the anhydrite reference sample to a water treatment that converted anhydrite to hydrated calcium sulfate, we observed that the fluorescence doublet becomes a single band around 320-330 nm, similar to the one observed in DER (Supplementary Fig. 2b). This supports an inorganic interpretation also for the co-located fluorescence observations in DER.

**Organics preservation by sulfates.** The observation of C-C and C=C ring stretching bands of PAHs instead of other bands typical of macromolecular carbon (MMC) and heavily altered organic matter widely found in Martian meteorites, specifically co-located with an aqueous mineral like sulfate, may be evidence of salt-mediated preservation of organic material. Terrestrial sulfate minerals have been shown to efficiently trap and preserve organic molecules within their structure<sup>24</sup>. Similarly, sulfate minerals are likely to preserve organic molecules from the oxidizing conditions on the Martian surface when trapped within intracrystalline inclusions<sup>25</sup>. In addition, magnesium sulfate has shown photoprotective properties<sup>26</sup>, which might have enabled the preservation of molecular features once QRT subsurface material was exposed to Martian ambient conditions after abrasion before being measured with SHERLOC on sol 293 and until sol 304, as indicated by the invariance in shape/position of the Raman features of interest in the spectra acquired 11 sols apart<sup>5</sup>. The same photoprotection mechanism might have occurred in the case of PMT once its natural surface was exposed to Martian UV irradiation after removal of dust using *Perseverance's* gas dust removal tool. The preservation provided by sulfates might have slowed down molecular degradation, maintaining an immature refractory organic material, featuring three- and two-ring aromatic moieties structurally similar to PAHs. In addition, C-C and C=C ring stretching bands of PAHs in the regions 1300-1500  $\text{cm}^{-1}$  and 1600-1700  $\text{cm}^{-1}$  exhibit very low detection limits due to resonance enhancement in DUV Raman, potentially obscuring bands of less resonantly enhanced compounds that also might be present in the samples. In contrast, C-H stretching bands around ~3000

cm<sup>-1</sup> are not resonantly enhanced and may also be suppressed by the local bonding environment within the sulfate phase. PAHs have also been found in Martian meteorites<sup>14</sup>, including the ~4-billion-year-old ALH84001 meteorite<sup>16</sup>, which suggests appreciable PAH accumulations in early Mars environments and implies that PAHs can withstand Martian and space conditions for billions of years. Moreover, the Sample Analysis at Mars (SAM) instrument onboard the NASA Mars Science Laboratory's (MSL) *Curiosity* rover detected PAHs at Gale crater on Mars, likely resulting from the fragmentation of MMC in the SAM instrument at high temperature<sup>33,37</sup>. Finally, the presence of three- and two-ring PAHs in the QRT and PMT targets aligns with chemical analyses of insoluble organic matter (IOM) found in meteorites, which suggest that IOM is composed of small PAH units, typically 1-3 rings, with short, highly branched aliphatic and ester chains<sup>38</sup>.

**Sample preparation.** The reference mineral phases used in this work are: magnesium sulfate heptahydrate ( $\geq 99.5\%$  purity, Sigma); magnesium sulfate monohydrate (97% purity, Sigma), which when measured by DUV Raman exhibited hydration features consistent with a mixture of magnesium sulfate mono- and dihydrate (Extended Data Fig. 1a); calcium sulfate ( $>99.99\%$  purity, Aldrich), which when measured by X-ray diffraction (XRD) turned out to be anhydrite with minor bassanite (Supplementary Fig. 3). The reference bassanite sample was synthesized first by converting the calcium sulfate ( $>99.99\%$  purity, Aldrich) into gypsum through water treatment and then heating the gypsum at 200°C for 24 hours<sup>39</sup>. The starkeyite reference sample was synthesized by Clark et al.<sup>40</sup> and its DUV Raman spectrum is reported in Siljeström et al.<sup>5</sup>. The anhydrite reference sample was synthesized by heating calcium sulfate dihydrate (98+% purity, ACROS) at 700°C for 48 hours, to simultaneously remove any potential organic carbon admixtures. Both abiotic organics expected on Mars and potential biotic organics were tested in this work, choosing a few representatives of different classes of aromatic organic compounds, including amino acids, nucleic acid components, pigments, carboxylic acids, small PAHs, and insoluble organic matter, to cover a broad spectrum of organics easily detectable by SHERLOC. The abiotic organics included: the carboxylic acids phthalic acid ( $\geq 99.5\%$  purity, Sigma-Aldrich), mellitic acid (99% purity, Aldrich), and benzoic acid ( $\geq 99.5\%$  purity, Sigma-Aldrich); the PAHs naphthalene (99% purity, Aldrich), benzo[a]pyrene (analytical standard, Supelco), 9-methylanthracene (98% purity, Aldrich), 1,3-dihydroxynaphthalene ( $\geq 99\%$  purity, Merck), 2,6-dihydroxynaphthalene (98% purity, Sigma-Aldrich), 1-naphthol (99+% purity, Aldrich) and 2-naphthol (99% purity, Sigma-Aldrich); a synthetic analog for the meteoritic insoluble organic matter (IOM); the benzothiophenes 1-benzothiophene ( $\geq 98\%$  purity, Sigma-Aldrich) and dibenzothiophene ( $\geq 99\%$  purity, Aldrich). The potential biotic organics included: the amino acids L-phenylalanine ( $\geq 98\%$  purity, Sigma-Aldrich), L-tyrosine ( $\geq 98\%$  purity, Sigma-Aldrich), L-tryptophan (98% purity, Sigma-Aldrich); the nucleic acid components uracil ( $\geq 99\%$  purity, Sigma-Aldrich), adenosine 5'-triphosphate disodium salt hydrate (ATP) ( $\geq 99\%$  purity, Sigma-Aldrich), adenosine 5'-monophosphate sodium salt (AMP) ( $\geq 99\%$  purity, Sigma), cytosine (98+% purity, Alfa Aesar), adenosine ( $\geq 99\%$  purity, Sigma), uridine 5'-monophosphate disodium salt (UMP) ( $\geq 99\%$  purity, Sigma), adenine hydrochloride (98+% purity, Alfa Aesar), guanine (98% purity, Aldrich). In addition, two oxy-PAH polymers were used, poly1-HN and poly1,8-DHN, synthesized by P. Manini and V. Lino starting from 1-naphthol (1-

HN) and 1,8-dihydroxynaphthalene (1,8-DHN), respectively. According to a procedure previously reported in the literature<sup>41,42</sup>, the polymers were prepared by following a standard protocol involving the oxidation of the proper monomer with the horseradish peroxidase (HRP)/H<sub>2</sub>O<sub>2</sub> system in 0.1 M phosphate buffer at pH 7.0. Since 1,8-DHN is a metabolite, its polymer can be considered a synthetic analogue of melanin produced by certain types of fungi. 1-HN, on the other hand, is not a metabolite, and therefore its polymer cannot be considered biotic. However, poly1-HN can be considered a polymer of astrochemical relevance since 1-HN is the product obtained by irradiating naphthalene in water ice<sup>43</sup>. The sample of synthetic insoluble organic matter (IOM) was prepared by P. Manini and V. Lino according to the procedure reported by Kebukawa et al.<sup>44</sup>. In brief, a mixture of paraformaldehyde and glycolaldehyde (2:1 molar ratio) was dissolved in water and treated with calcium hydroxide (Ca(OH)<sub>2</sub>) and ammonia. The reaction mixture was subjected to microwave irradiation for 30 minutes at 160 °C. After the reaction time, a dark solid was formed; this latter was isolated by centrifugation, washed with 2 M HCl to remove the calcium ions and freeze dried. To simulate the interaction of organic molecules with hydrated magnesium sulfate, as inferred from QRT observations, a set of 27 organo-sulfate analog samples was prepared by equilibrium adsorption of 1 wt% organic molecules on hydrated magnesium sulfate, following a procedure developed by Fornaro et al.<sup>5</sup>. A 1 wt% doping was chosen to ensure a clear organic detection over any minor contaminants that may occur in the samples. Specifically, organics were dissolved/suspended in milli-Q water and mixed with the purest hydrated magnesium sulfate available, i.e., magnesium sulfate heptahydrate (≥99.5% purity, Sigma), for about 24 hours in order to reach steady state equilibrium and allow the establishment of molecule-mineral interactions; then, the suspensions were dried in oven at 40°C to simulate desiccation of a possible liquid water body on Mars, obtaining organics-doped magnesium sulfate samples with various hydration states depending on the specific organic molecule as indicated by differences in deep UV Raman features<sup>45</sup>. In the case of naphthalene and 1-benzothiophene, which are highly volatile, toluene and methanol were used as solvents, respectively, to dry the samples more quickly and avoid complete evaporation of organic molecules during desiccation.

**Deep UV (DUV) Raman and fluorescence analog instruments.** Samples were characterized with laboratory instruments analogous to SHERLOC. These included the “Analogue Complementary Raman for Operations on Mars” (ACRONM) instrument located at NASA’s Johnson Space Center, the Brassboard instrument located at the Jet Propulsion Laboratory, and the Photon Systems RPL200 instrument located at INAF-Astrophysical Observatory of Arcetri, operated to mimic SHERLOC analysis. All three instruments utilize DUV excitation (248.6 nm) from a NeCu pulsed laser. Brassboard spectra were acquired using from 5 to 800 pulses per point, 15-20 A laser current, and were averaged over 25 points (5x5 map). Cosmic rays were removed, and data was laser normalized using an open-source software package named Loupe (Version V5.1.5) developed at the NASA Jet Propulsion Laboratory by K. Uckert<sup>46</sup>, and adjusted using a custom Python script based on acetonitrile for calibration. Raman data were baselined with a modified asymmetric least squares algorithm. More details about the Brassboard configuration and operations can be found in Razzell Hollis et al.<sup>47</sup>. ACRONM Raman spectra were acquired using 1200 pulses per point and averaged over three

independent measurements at different sample locations, while fluorescence spectra were acquired using a few to tens of pulses per point (because the fluorescence is much stronger than Raman) and averaged over ten independent measurements at different sample locations. Spectral baselining was performed, only when required, by fitting the background to the lowest order polynomial needed for an adequate fit. A description of the ACRONM instrument can be found in Siljeström et al.<sup>5</sup>. Photon Systems RPL200 Raman and fluorescence spectra were acquired using 100 and 1-10 pulses per point, respectively, 20 A laser current and a repetition rate of 40 pulses per second, which enable it to reproduce the same performance as SHERLOC using a 5X microscope objective, and averaged over hundreds of points. Specifically, the reference samples of anhydrite with minor bassanite and magnesium sulfate monohydrate, and the hydrated magnesium sulfate doped with dibenzothiophene were analyzed with the Brassboard instrument. The reference samples of starkeyite and anhydrite with minor bassanite, and magnesium sulfate doped with phthalic acid, mellitic acid, naphthalene, benzo[a]pyrene, 9-methylanthracene, 2,6-dihydroxynaphthalene, 1-naphthol, 2-naphthol, IOM, dibenzothiophene, L-phenylalanine, L-tyrosine, L-tryptophan, uracil, ATP, AMP, cytosine, adenosine, UMP, adenine hydrochloride, guanine, poly1-HN and poly1,8-DHN were analyzed with the ACRONM instrument. The reference samples of bassanite and gypsum, the hydrated magnesium sulfate water blank and the hydrated magnesium sulfate doped with benzoic acid, 1,3-DHN and 1-benzothiophene were analyzed with the RPL200 instrument. In addition, the anhydrite reference spectrum was measured using the MORIARTI instrument (Mineralogy and Organics Raman Instrumentation for the Analysis of Terrestrial Illumination) located at the University of Pittsburgh, which is a custom DUV Raman microscope coupled with several spectrometers to cover the entire Raman and fluorescence (UV and visible light) spectral range<sup>2</sup>. Samples can be illuminated with a Coherent Industries Innova 300 FreD frequency-doubled Ar<sup>+</sup> laser (248.3 nm, roughly 10 mW average power). Laser light passes through a 248.6 nm laser clean up filter before being focused onto a turning prism and directed onto the sample as a roughly 120 μm diameter spot. Scattered and emitted light is collected in a 180° backscatter geometry using an f1.25 reflective cassegrain objective and passes through a Semrock 248 nm long-pass filter before entering one of the spectrometers. For Raman, light is dispersed from 250 to 278 nm to a resolution of 15 cm<sup>-1</sup> (100 μm slit) inside an f/6.8 Czerny–Turner spectrograph and focused onto a Princeton Instruments liquid nitrogen-cooled Pylon 400B CCD. The sample can also be illuminated by a halogen white light, in which it is imaged onto a 1.6MP Thorlabs CMOS camera. SHERLOC and the four analog instruments all have significantly different spectrometer slit functions that contribute width to the Raman bands observed in the spectrum. As a result, Raman spectra of the same sample can differ between the instruments. To compare Raman bandwidths across instruments, we performed a calibration to account for the different spectrometer slit functions of the instruments<sup>48</sup>. The calculation of an instrument slit function involves measuring the observed Raman band (ORB) of a material with a known intrinsic Raman band (IRB) and performing a deconvolution to separate the slit function and the IRB from the ORB. A standard Teflon sample from the same batch of material with a known IRB was used to determine the slit function for all SHERLOC analog instruments using the procedure of Jakubek et al.<sup>48</sup>. The slit functions of SHERLOC, the Brassboard instrument, ACRONM, the RPL200, and the MORIARTI instruments are  $34.1 \pm 2$ ,  $44.0 \pm 0.6$ ,  $19.6 \pm 0.8$ ,  $25.3$

$\pm 0.6$ , and  $14.5 \pm 0.9 \text{ cm}^{-1}$ . With the slit functions for each instrument, the true intrinsic Raman bandwidth of each sample can be calculated by deconvolving the slit functions from an ORB from an instrument measurement<sup>48</sup> and bandwidths can be compared across instruments. While sample information, such as structural and environmental heterogeneity, can be extracted from calibrated Raman bandwidths, this is detailed work beyond the scope of this manuscript. Detailed data showing the relationship between all parameters used in calculating IRB are reported in the Supplementary Information (Supplementary Tables 1-4) and a detailed discussion of the bandwidth calibration procedure is provided in Jakubek et al.<sup>48</sup>.

**XRD analysis.** X-Ray diffraction pattern of the calcium sulfate sample (>99.99% purity, Aldrich) was collected on a Rigaku MiniFlex 6G benchtop instrument with a Co K $\alpha$  source (running at 40 kV and 15mA) with spectra collected from  $3^\circ 2\theta$  to  $70^\circ 2\theta$  at a scan rate of  $1.0^\circ 2\theta/\text{min}$ . The XRD instrument is located in the X-Ray Diffraction Laboratory at the NASA Johnson Space Center (JSC) where the sample was loaded onto 0.2 mm diameter well sample cups prior to analysis. HighScore Plus software (Malvern Panalytical) was used to analyze diffraction patterns and assist in mineral identification.

**ICP-MS analysis.** Cerium concentration of the calcium sulfate sample (>99.99% purity, Aldrich) was determined via solution analysis on a Thermo Fisher ElementXR ICP-MS at ARES NASA Johnson Space Center in the Center for Isotope Cosmochemistry & Geochronology. The sample was weighed (18 mg) into a 7 mL acid cleaned PFA beaker and dissolved in 3 mL of 6 N HCl (2x distilled) on a hotplate at  $120^\circ \text{C}$  for 24 hours. Upon visual inspection of a clear solution, the sample was dried down and reconstituted in 2% HNO<sub>3</sub> for cerium concentration analysis. The quantification of cerium concentration was carried out using a serial dilution of a Claritas PPT Grade ICP-MS Multi-Element Solution 1 calibration standard.

**SHERLOC data acquisition.** SHERLOC is an arm-mounted Raman and fluorescence spectrometer with a 248.6 nm NeCu deep-ultraviolet (DUV) pulsed laser excitation source (40  $\mu\text{s}$  pulse width). It has two cameras, the Wide Angle Topographic Sensor for Operations and eNginEering (WATSON) and the Autofocus Context Imager (ACI), which provide color context and spectrometer-boresighted images, respectively. The instrument is capable of mapping the surface of rocks and dust at a high spatial resolution of 100  $\mu\text{m}$  and nominal standoff of 48 mm<sup>49</sup>. SHERLOC can obtain multiple types of scans, including High Dynamic range (HDR, 10 x 10 point grid, 7 mm x 7 mm, 500 pulses per point), detail (10 x 10 point grid, 1 mm x 1 mm, 500 pulses per point), and survey scans (36 x 36 point grid, 5 mm x 5 mm, 15-20 pulses per point). The specific scans analyzed in this work are in the Supplementary Table 5. The colorized ACIs presented here are compositions of co-registered WATSON and ACI images of the same targets<sup>50</sup>.

**PIXL data acquisition.** PIXL is an arm-mounted microfocus X-ray fluorescence mapping spectrometer. X-rays are produced by a Rh tube and focused to  $\sim 120 \mu\text{m}$ <sup>51</sup> using a polycapillary optic. The instrument is scanned over the target surface using a hexapod to produce maps comprising several thousand discrete analytical spots

over areas around 0.5 cm<sup>2</sup> and a sampling interval of approximately 125 μm<sup>51</sup>. Scans are co-aligned with multispectral images collected with an integrated context camera at ~50 μm resolution. PIXL incorporates two X-ray detectors, allowing diffraction to be separated from fluorescence<sup>52,53</sup>. The scans analyzed in this work were collected from the same general target areas as the SHERLOC scans described earlier, and mapped approximately rectangular regions with dimensions 5 mm × 7 mm (Quartier, sol 294), 3.5 mm × 11 mm (Dragon's Egg Rock, sol 865), and 2 mm × 10 mm (Pilot Mountain, sol 874). All PIXL data were visualized and analyzed using PIXLISE and PIQUANT<sup>51</sup>. Spectra were processed using PIQUANT to estimate quantitative oxide abundances at each analytical spot<sup>54</sup> and post-processed using custom expressions in PIXLISE to correct for the effects of diffraction and rock surface roughness<sup>55</sup>. Quantified and corrected oxide abundance maps were subsequently visualized and exported using PIXLISE.

**Spectral data processing.** For SHERLOC data, preliminary spectral data processing was performed using an open-source software package named Loupe developed at the NASA Jet Propulsion Laboratory by K. Uckert. This software enables dark frame subtraction, laser normalization and the correlation of individual spectra to locations on the ACI image based on the scanning mirror positioning. Exported Loupe data were then further processed using MATLAB R2022a software (MATLAB Version: 9.12.0.1975300 Update 3), to perform cosmic ray removal when necessary, baseline subtraction using a second-order polynomial, and peak fitting with Voigt functions<sup>48</sup> in a semi-automated manner thanks to a script named SherlocFitAnalyzer developed by G. Poggiali, which allows evaluation of peak positions, peak heights and areas, and FWHM. The Raman bandshape is a result of the contribution of the instrument slit function and inhomogeneous broadening on the natural Lorentzian Raman lineshape<sup>48</sup>. The use of a Voigt function allows for adequate fitting for all Raman bandshapes observed across SHERLOC and the analog instruments. Signal-to-noise ratio (SNR) was calculated by dividing the fitted peak heights by the standard deviation of the population spectral noise between 2000 and 2100 cm<sup>-1</sup> for each spectrum. Requirements for SHERLOC Raman peak detection included FWHM equal or greater than SHERLOC spectral resolution (34 cm<sup>-1</sup>)<sup>49</sup> and SNR > 3. Data acquired with laboratory analog instruments were processed directly with MATLAB using the same script. All Voigt fit outcomes are reported in detail in the Supplementary Information (Supplementary Tables 6-16 and Supplementary Figures 4-14).

**Computational spectroscopy simulations.** Quantum chemical calculations were performed for the target molecules 1,3-DHN, 2,6-DHN and 9-MA, in order to simulate their vibrational features and support the assignment of the experimental spectra in terms of molecular normal modes of vibration. On the basis of the recent literature on the subject<sup>56</sup>, the double-hybrid functional DSDPBEP86<sup>57</sup> in conjunction with the ju-cc-pVTZ basis set<sup>58</sup>, and the PW6B95<sup>59</sup> meta-hybrid functional coupled with the jul-cc-pVDZ basis set were the levels of theory of choice to predict the spectroscopic properties of 1,3- and 2,6-DHN (molecular structures with atom labelling are provided in the Supplementary Fig. 15). In the case of the larger 9-MA molecule, the B3LYP hybrid functional<sup>60</sup>, in conjunction with the jul-cc-pVDZ basis set, was used because of the lower

computational cost. All density functionals were augmented for dispersion interactions through the DFT-D3<sup>61</sup> scheme with Becke-Johnson damping<sup>62</sup>. Geometry optimizations were carried out at first using very tight convergence criteria and then analytical Hessians and dipole moment first derivatives were evaluated at the optimal geometries to obtain vibrational harmonic frequencies, infrared intensities and Raman activities. In the case of PW6B95 and B3LYP computations, anharmonic contributions to the transition frequencies (i.e. cubic and semi-diagonal quartic force constants) and IR intensities/Raman activities (second and third derivatives of the property surface) were evaluated by numerical differentiation of analytic quadratic force constants and dipole moment first derivatives, respectively. These quantities were then used to derive transition frequencies, infrared intensities and Raman activities beyond the double-harmonic approximation within the framework of second-order vibrational perturbation theory (VPT2)<sup>63</sup>. Specifically, in the case of 1,3- and 2,6-DHN, a hybrid force field<sup>64</sup> was devised by mixing the DSDPBEP86-D3/jun-cc-pVTZ harmonic force field with anharmonic contributions evaluated at the PW6B95-D3/jul-cc-pVDZ, while in the case of 9-MA, VPT2 was applied on top of the anharmonic force field fully evaluated at the B3LYP-D3/jul-cc-pVDZ level of theory. In order to overcome the problem of Fermi interactions affecting the computation of vibrational energies and intensities, Generalized VPT2 was employed<sup>65</sup>. According to this approach, divergent terms are identified and removed from the perturbative equations and then, the interaction is treated in a second step of reduced dimensionality by setting up and diagonalizing the proper interaction matrix. In the case of 9-MA, the lowest lying fundamental vibrations behave as large amplitude motions (LAMs), for which a fourth-order expansion of the potential energy surface, upon which VPT2 relies, can provide unrealistic anharmonic corrections. To avoid contamination from LAMs into the remaining small amplitude vibrations, a reduced dimensionality approach<sup>66</sup> was adopted in which LAMs were decoupled and treated at the harmonic level. Measured fingerprints were interpreted based on the calculations performed for the free non-interacting molecule. At first, the experimental DRIFT and Raman spectra of the pure compounds were assigned under the guidance of the simulated bandshapes. Then, comparison between the DUV Raman spectra of the molecule pure and interacting with magnesium sulfate led to the identification of the bands of the organo-sulfate adducts in terms of normal modes of vibrations. While more refined simulations based on atomistic models for the interaction of PAHs with sulfate minerals are being investigated at the STARK laboratory, and accurate simulations of resonance Raman spectra will be the subject of a dedicated work, it should be noted that the presented simulations represent a good approximation because the CC stretching fundamentals are usually subjected to the strongest enhancements in DUV Raman spectroscopy. The computed vibrational frequencies and relative assignments for the features of interest of 1,3-DHN, 2,6-DHN and 9MA are reported in Supplementary Table 17.

**Data availability.** The Mars 2020 mission data used for this study are available on the Planetary Data System (PDS) at <https://pds.nasa.gov/>. Data from the SHERLOC instrument are accessible at <https://pds-geosciences.wustl.edu/missions/mars2020/sherloc.htm>, organized by sol number and accessible in csv format at [https://pds-geosciences.wustl.edu/m2020/urn-nasa-pds-mars2020\\_sherloc/data\\_processed/](https://pds-geosciences.wustl.edu/m2020/urn-nasa-pds-mars2020_sherloc/data_processed/). Fundamental

data record image data acquired by the ACI are organized by sol number and accessible in IMG format at [https://pds-imaging.jpl.nasa.gov/data/mars2020/mars2020\\_imgops/data\\_aci\\_imgops/sol/](https://pds-imaging.jpl.nasa.gov/data/mars2020/mars2020_imgops/data_aci_imgops/sol/). DUV Raman and fluorescence spectra of organo-sulfate analogs and reference sulfates are publicly accessible through the Open Data Repository's (ODR) Data Publisher platform<sup>45</sup>.

**Code availability.** PIXLISE and PIQUANT are available as open-source software under the Apache License 2.0 at <https://github.com/pixlise>. The code for ACI colorization is available under the Apache 2.0 licence at <https://github.com/nasa-jpl/ACI-colorization>. Loupe software is open source under the Apache 2.0 licence and available at <https://github.com/nasa/Loupe>. SherlocFitAnalyzer script is open source under the GNU GENERAL PUBLIC LICENSE Version 3 and available at <https://github.com/giopoggiali/SherlocFitAnalyzer>.

### **Acknowledgements**

The authors thank the SHERLOC, PIXL and Mars 2020 science and engineering teams for acquisition of the data that enabled this study. This research was supported by the Italian Space Agency (ASI) through the ASI/INAF agreement no. 2023-3-HH, and by European Union—Next Generation EU through the PRIN MUR 2022 “Experimental and computational analog studies to support identification of organics on Mars by the NASA Mars 2020 Perseverance rover”. In addition, T.F. was supported by INAF through Mini Grant Ricerca Fondamentale INAF 2022. Research efforts carried out at the Jet Propulsion Laboratory, California Institute of Technology by K.H., S.Sh., and K.U. were funded under a contract with the National Aeronautics and Space Administration (80NM0018D0004). A.E.M. was funded by the Mars 2020 Program through Planetary Science Institute subcontract 1641753. K.C.B. was funded under a contract with the National Aeronautics and Space Administration (80NSSC20K0235). N.C.H. and R.V.M. were supported in part by the ISFM Mission Enabling Work Package at the Johnson Space Center. W.P.B. and J.I.S. were supported in part by the ISFM Geochemistry and Cosmochemistry Work Package at the Johnson Space Center. E.A.C. was funded by grants from the Canadian Space Agency (22EXPCOI4) and the Natural Sciences and Engineering Research Council of Canada (RGPIN-2023-03413). Y.P. was supported by funds to the SHERLOC instrument team. S.S. was supported by the Swedish National Space Board (2021-00092). S.A.C. and R.C.W. were funded by JPL contract 1688677 for SHERLOC. M.E.M. was funded under a contract to the Jet Propulsion Laboratory (1703459). The STARK group is acknowledged for high-performance computing facilities.

### **Author contributions**

T.F. analyzed and interpreted both SHERLOC and laboratory analog data, and wrote the manuscript and supplementary material. S.Sh., R.S.J., A.E.M., R.B., A.A., S.B., C.G.F., F.R., S.V.B. measured the laboratory analog samples with SHERLOC-like instruments. G.P. developed the SherlocFitAnalyzer script to analyze both SHERLOC and laboratory analog data. M.T. analyzed and interpreted PIXL data. Y.P. provided the list of sulfate detections in the Jezero crater floor and fan. N.C.H. and R.V.M. performed the XRD characterization. J.I.S. and W.P.B. performed the ICPMS analysis. V.L. and P.M. synthesized the two oxy-PAH polymers and

the IOM. N.T. and D.A.-J. carried out the computational simulations. All co-authors participated in data analysis, processing, discussion and interpretation of results and/or manuscript editing.

### Competing interests

The authors declare no competing interests.

**Table 1. Cross-comparison of peak parameters for the features of interest in Quartier, Pilot Mountain and Dragon’s Egg Rock with organo-sulfate analogs.** Comparison of peak positions, full-width at half-maxima (FWHM, calibrated with respect to SHERLOC spectral resolution in case of laboratory data), and peak height (I) ratios of the Raman features of organo-sulfate analogs and sulfates with those observed in Quartier (average of the Raman spectra of point 34 of HDR scan from sol 293 and points 45, 46 and 77 of detail 1 scan from sol 304), Pilot Mountain (average of the Raman spectra of points 30 and 31 of detail 1 scan from sol 874), and Dragon’s Egg Rock (average Raman spectrum of the full map of detail 1 scan from sol 861), obtained by Voigt fit. Shifts of peak position ( $\Delta$ ,  $\text{cm}^{-1}$ ) with respect to SHERLOC observations are also reported. Best matches are reported in bold.

	Peak Position ( $\text{cm}^{-1}$ )	FWHM ( $\text{cm}^{-1}$ )	Peak Height Ratios	Peak Position ( $\text{cm}^{-1}$ )	FWHM ( $\text{cm}^{-1}$ )	Peak Height Ratios
Quartier	1340	~70	$I_{1340}/I_{1643}=2$ $I_{1010(\text{v}1)}/I_{1340}=35$	1643	~42	$I_{3399(\text{vOH})}/I_{1643}=3$
	1395	~39	$I_{1395}/I_{1643}=2$			
	1440	~80				
9-MA-MgSulfate	1402 ( $\Delta_{1395}=7$ )	~36	$I_{1402}/I_{1618}=2$	1618 ( $\Delta_{1643}=-25$ )	~37	
2,6-DHN-MgSulfate	1370 ( $\Delta_{1395}=-25$ )	~49	$I_{1370}/I_{1610}=1$	1610 ( $\Delta_{1643}=-33$ )	>60	
1,3-DHN-MgSulfate	1391 ( $\Delta_{1395}=-4$ )	~43	$I_{1391}/I_{1627}=1$	1627 ( $\Delta_{1643}=-16$ )	~48	
Anhydrite	1359 ( $\Delta_{1340}=19$ )	~46	$I_{1016(\text{v}1)}/I_{1359}=445$			
Magnesium sulfate mono/dihydrate				1513 ( $\Delta_{1643}=-130$ )	>60	$I_{3201(\text{vOH})}/I_{1513(\delta\text{OH})}=5$
Starkeyite				1599 ( $\Delta_{1643}=-44$ )	~50	$I_{3410(\text{vOH})}/I_{1599(\delta\text{OH})}=19$
Pilot Mountain	1360	60	$I_{1360}/I_{1646}=2$ $I_{1015(\text{v}1)}/I_{1360}=33$	1646	~70	$I_{3539(\text{vOH})}/I_{1646}=2$

	<b>1410</b>	~ <b>60</b>	<b>I<sub>1410</sub>/I<sub>1646</sub>=2</b>			
	1480	~50				
9-MA-MgSulfate	<b>1402</b> ( $\Delta_{1410}=-8$ )	~36	<b>I<sub>1402</sub>/I<sub>1618</sub>=2</b>	1618 ( $\Delta_{1646}=-28$ )	~37	
2,6-DHN-MgSulfate	1370 ( $\Delta_{1360}=10$ )	~49	$I_{1370}/I_{1610}=1$	1610 ( $\Delta_{1646}=-36$ )	>60	
1,3-DHN-MgSulfate	1391 ( $\Delta_{1410}=-19$ )	~43	$I_{1391}/I_{1627}=1$	<b>1627</b> ( $\Delta_{1646}=-19$ )	~48	
Anhydrite with minor bassanite	1357 ( $\Delta_{1360}=-3$ )	~35	$I_{1357}/I_{1621}=1$ $I_{1013(v1)}/I_{1357}=313$	1621 ( $\Delta_{1646}=-25$ )	>60	$I_{3564(vOH)}/I_{1621(\delta OH)}=9$
<b>Dragon's Egg Rock</b>	<b>1339</b>	~ <b>45</b>	<b>I<sub>1339</sub>/I<sub>1631</sub>=1</b> <b>I<sub>1013(v1)}/I<sub>1339</sub>=217</sub></b>	<b>1631</b>	~ <b>46</b>	<b>I<sub>3534(vOH)}/I<sub>1631</sub>=31</sub></b>
	<b>1403</b>	~ <b>74</b>	<b>I<sub>1403</sub>/I<sub>1631</sub>=1</b>			
9-MA-MgSulfate	1402 ( $\Delta_{1403}=-1$ )	~36	$I_{1402}/I_{1618}=2$	1618 ( $\Delta_{1631}=-13$ )	~37	
2,6-DHN-MgSulfate	1370 ( $\Delta_{1339}=31$ )	~49	$I_{1370}/I_{1610}=1$	1610 ( $\Delta_{1631}=-21$ )	>60	
1,3-DHN-MgSulfate	<b>1391</b> ( $\Delta_{1403}=-12$ )	~43	<b>I<sub>1391</sub>/I<sub>1627</sub>=1</b>	<b>1627</b> ( $\Delta_{1631}=-4$ )	~ <b>48</b>	
Bassanite	<b>1333</b> ( $\Delta_{1339}=-6$ )	>60	<b>I<sub>1333</sub>/I<sub>1619</sub>=1</b> <b>I<sub>1006(v1)}/I<sub>1333</sub>=225</sub></b>	<b>1619</b> ( $\Delta_{1631}=-12$ )	>60	<b>I<sub>3530(vOH)}/I<sub>1619(\delta OH)</sub>=24</sub></b>

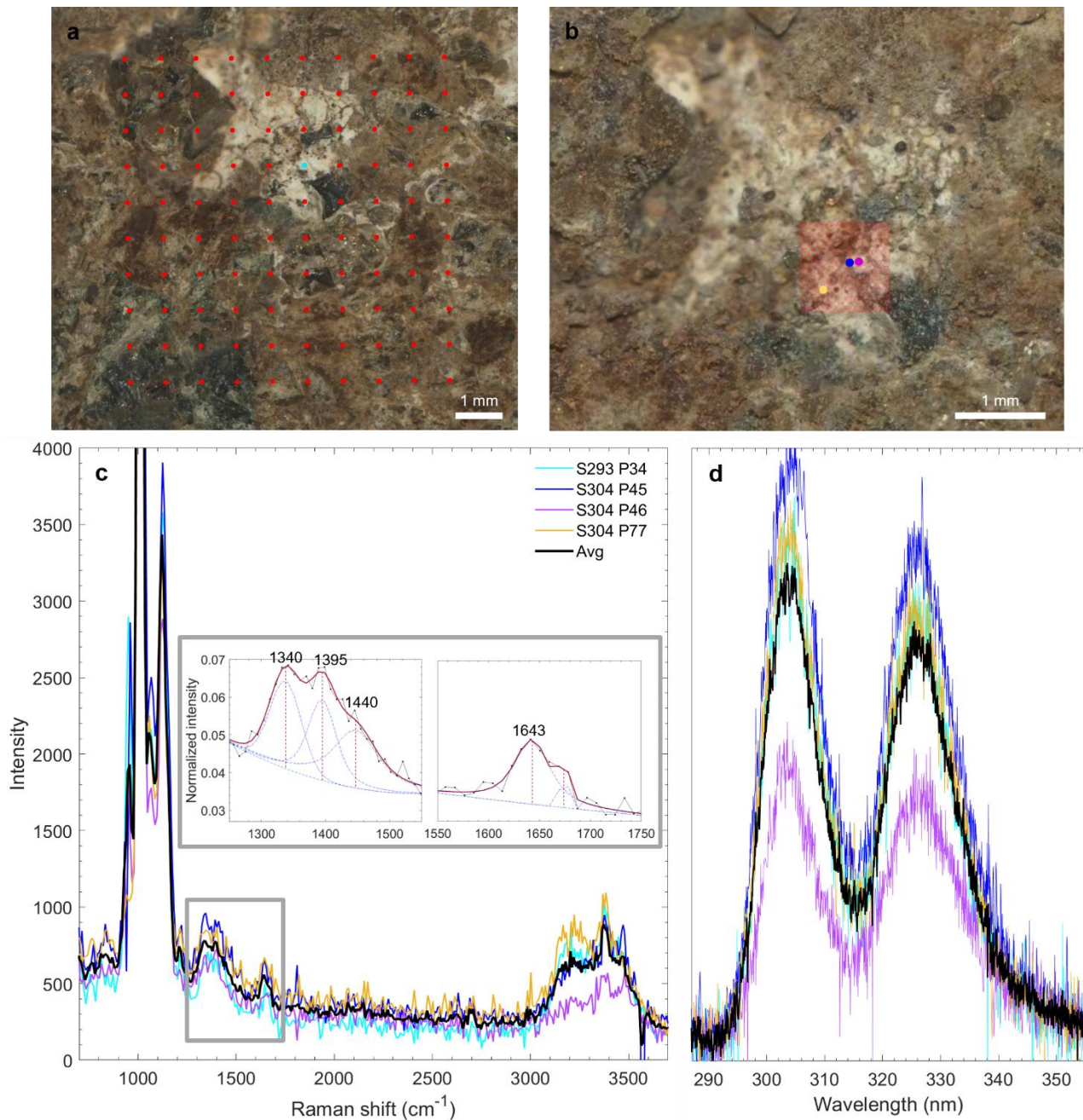


**Fig. 1. Raman features in the spectral ranges relevant to organics and co-located fluorescence in Quartier.** **a**, Colorized ACI image of a region where a high dynamic range (HDR) scan ( $10 \times 10$  points over  $7 \times 7 \text{ mm}^2$ ) was performed on the Quartier target on sol 293. Red dots with the same diameter of the laser beam represent locations where SHERLOC measurements were performed. Cyan dot corresponds to point 34, where the Raman features of interest were detected. **b**, Colorized ACI image of a region where the detail 1 scan ( $10 \times 10$  points over  $1 \times 1 \text{ mm}^2$ ) was performed on the Quartier target on sol 304. Blue, purple, and yellow dots correspond to points 45, 46 and 77, respectively, where the Raman features of interest were detected. **c**, Raman spectra of point 34 of HDR scan from sol 293 (cyan), and points 45 (blue), 46 (purple) and 77 (yellow) of detail 1 scan from sol 304, along with their average (black). Inset shows Voigt fitting in the spectral ranges relevant to organics of the average spectrum normalized on the main anhydrite peak that enabled to identify the peaks at  $1340 \pm 4 \text{ cm}^{-1}$  (SNR 11, FWHM  $70 \pm 20 \text{ cm}^{-1}$ , area  $1.69 \pm 0.08$ , height  $0.0269 \pm 0.0002$ ),  $1395 \pm 2 \text{ cm}^{-1}$

(SNR 12, FWHM  $39 \pm 5 \text{ cm}^{-1}$ , area  $1.08 \pm 0.02$ , height  $0.02852 \pm 0.00004$ ),  $1440 \pm 40 \text{ cm}^{-1}$  (SNR 7, FWHM  $80 \pm 30 \text{ cm}^{-1}$ , area  $1.31 \pm 0.09$ , height  $0.018 \pm 0.005$ ) and  $1643.4 \pm 0.2 \text{ cm}^{-1}$  (SNR 7, FWHM  $42 \pm 4 \text{ cm}^{-1}$ , area  $0.94 \pm 0.03$ , height  $0.0171 \pm 0.0002$ ). In the inset, the unfitted average spectrum normalized on the main anhydrite peak (black), fitted spectrum (red) and baseline (blue) are shown. **d**, Fluorescence spectra of point 34 of HDR scan from sol 293 (cyan), and points 45 (blue), 46 (purple) and 77 (yellow) of detail 1 scan from sol 304, along with their average (black), exhibiting a doublet at  $\sim 303$  and  $325 \text{ nm}$ .

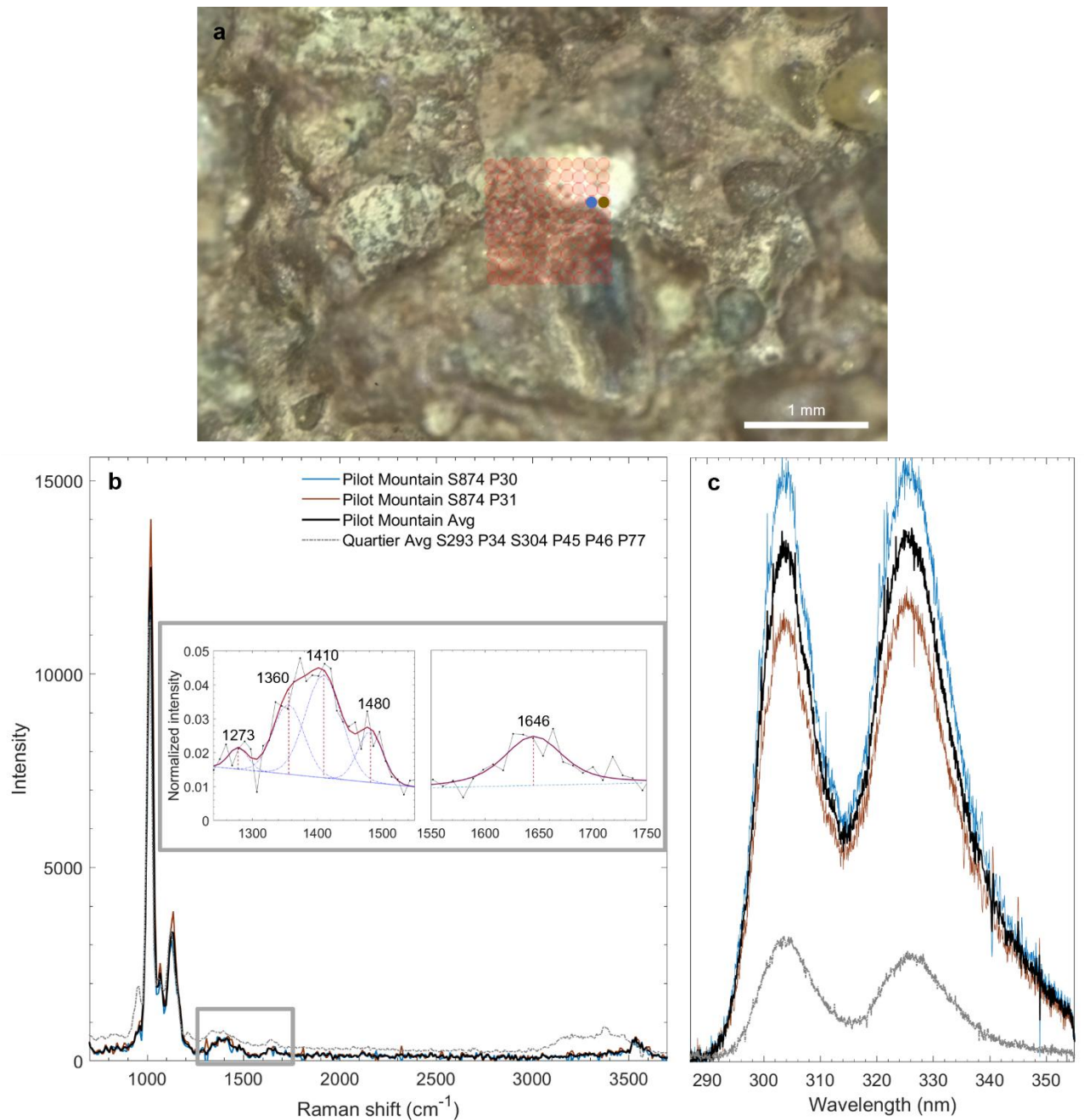


**Fig. 2. Raman features in the spectral ranges relevant to organics and co-located fluorescence in Pilot Mountain.** **a**, Colorized ACI image of a region where the detail 1 scan ( $10 \times 10$  points over  $1 \times 1 \text{ mm}^2$ ) was performed on the Pilot Mountain target on sol 874. Red dots with the same diameter of the laser beam represent locations where SHERLOC measurements were performed. Blue and brown dots correspond to points 30 and 31, respectively, where the Raman features of interest were detected. **b**, Raman spectra of points 30 (blue) and 31 (brown) of detail 1 scan from sol 874, along with their average (black), compared with the average of the Raman spectra of point 34 of HDR scan from sol 293 and points 45, 46 and 77 of detail 1 scan from sol 304 in Quartier (dashed grey). Inset shows Voigt fitting in the spectral ranges relevant to organics of the average spectrum normalized on the main calcium sulfate peak that enabled to identify the peaks at  $1273 \pm 5 \text{ cm}^{-1}$  (SNR 5, FWHM  $50 \pm 90 \text{ cm}^{-1}$ , area  $0.4 \pm 0.3$ , height  $0.009 \pm 0.002$ ),  $1360 \pm 90 \text{ cm}^{-1}$  (SNR 17, FWHM  $60 \pm 200 \text{ cm}^{-1}$ , area  $1.5 \pm 0.4$ , height  $0.03 \pm 0.01$ ),  $1410 \pm 50 \text{ cm}^{-1}$  (SNR 20, FWHM  $60 \pm 100 \text{ cm}^{-1}$ , area  $2.3 \pm 0.2$ , height  $0.034 \pm 0.007$ ),

1480±20 cm<sup>-1</sup> (SNR 10, FWHM 50±100 cm<sup>-1</sup>, area 0.8±0.2, height 0.017±0.003), and 1646±7 cm<sup>-1</sup> (SNR 10, FWHM 70±40 cm<sup>-1</sup>, area 1.1±0.1, height 0.014±0.002). In the inset, the unfitted average spectrum normalized on the main calcium sulfate peak (black), fitted spectrum (red) and baseline (blue) are shown. **c**, Fluorescence spectra of points 30 (blue) and 31 (brown) of detail 1 scan from sol 874, along with their average (back) compared with the average of the fluorescence spectra of the points of interest in Quartier (dashed grey), exhibiting a doublet at ~303 and 325 nm.

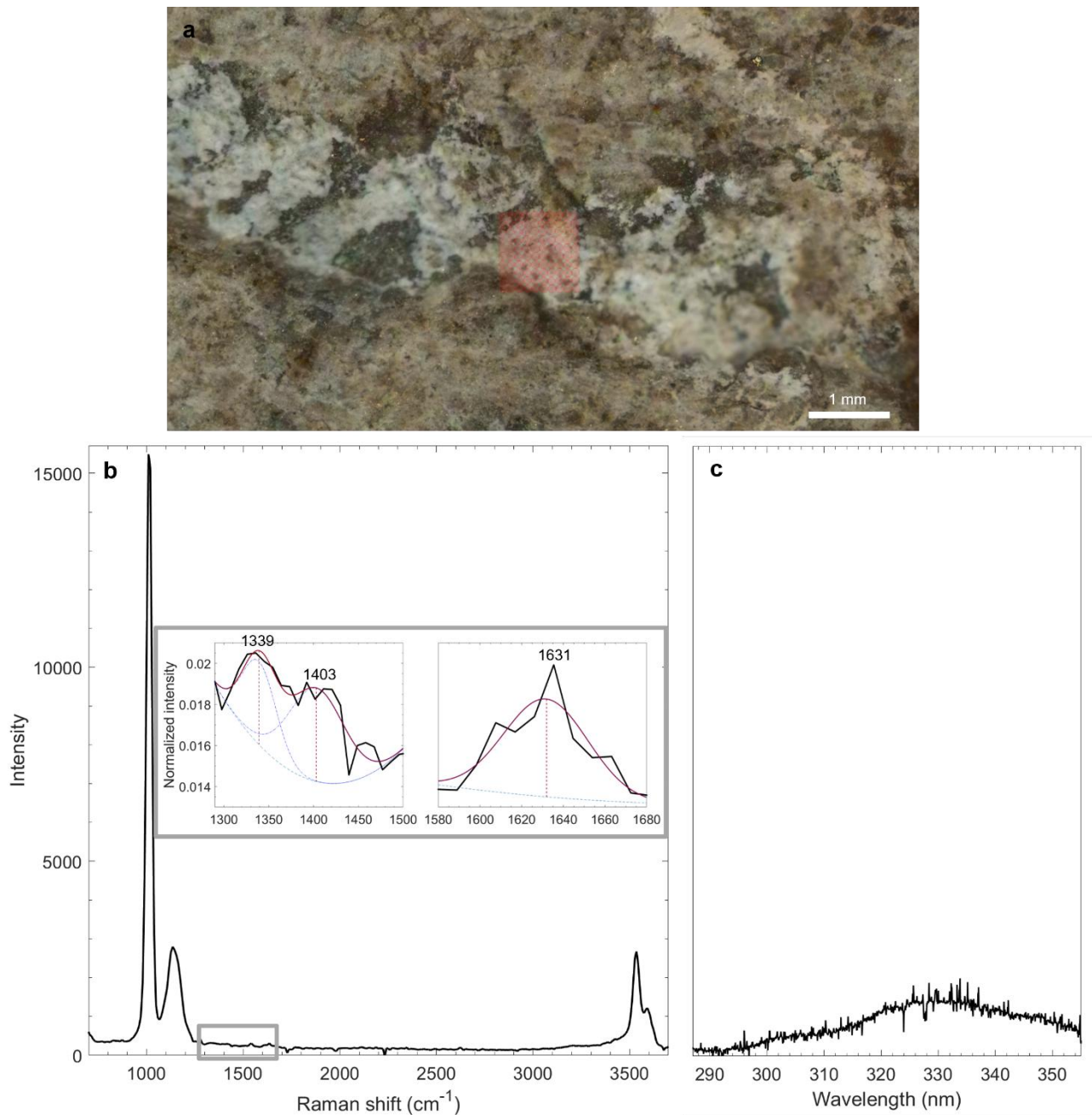


**Fig. 3. Raman features in the spectral ranges relevant to organics and co-located fluorescence in Dragon's Egg Rock.** **a**, Colorized ACI image of a region where the detail 1 scan ( $10 \times 10$  points over  $1 \times 1 \text{ mm}^2$ ) was performed on the Dragon's Egg Rock target on sol 861. Red dots with the same diameter of the laser beam represent locations where SHERLOC measurements were performed. **b**, Average Raman spectrum of the full map of detail 1 scan from sol 861. Inset shows Voigt fitting in the spectral ranges relevant to organics of the average spectrum normalized on the main calcium sulfate peak that enabled to identify the peaks at  $1338.813 \pm 0.002 \text{ cm}^{-1}$  (SNR 14, FWHM  $45 \pm 3 \text{ cm}^{-1}$ , area  $0.19 \pm 0.02$ , height  $0.0045 \pm 0.0001$ ),  $1403.125 \pm 0.001 \text{ cm}^{-1}$  (SNR 14, FWHM  $73.5 \pm 0.4 \text{ cm}^{-1}$ , area  $0.35 \pm 0.03$ , height  $0.0045 \pm 0.0001$ ), and  $1630.521 \pm 0.003 \text{ cm}^{-1}$  (SNR 15, FWHM  $46 \pm 6 \text{ cm}^{-1}$ , area  $0.23 \pm 0.04$ , height  $0.00478$ ). In the inset, the unfitted average spectrum normalized on the main calcium sulfate peak (black), fitted spectrum (red) and baseline (blue) are shown. **c**, Average fluorescence spectrum of the full map of detail 1 scan from sol 861.

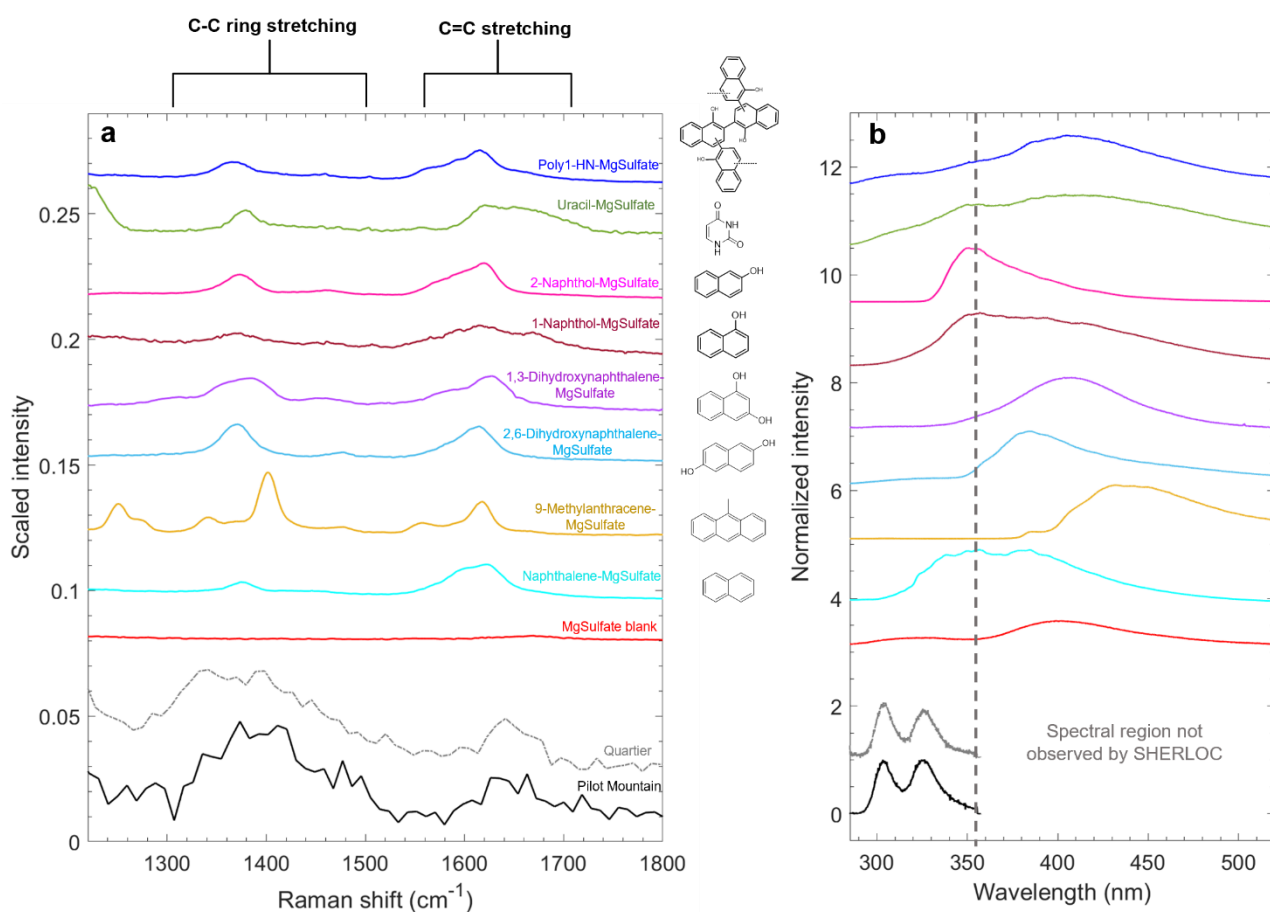


**Fig. 4. Cross-comparison of the features of interest in Quartier and Pilot Mountain with spectra of organo-sulfate analogs.** **a**, Average of Raman spectra of points 30 and 31 of detail 1 scan from sol 874 in Pilot Mountain (solid black), and average of Raman spectra of point 34 of HDR scan from sol 293 and points 45, 46 and 77 of detail 1 scan from sol 304 in Quartier (dashed grey), normalized on the main peak of calcium sulfate, compared with the Raman spectrum of hydrated magnesium sulfate water blank (red), scaled with respect to Quartier's hydration features and offset for clarity, and the Raman spectra of hydrated magnesium sulfate doped with: naphthalene (cyan), 9-methylanthracene (9-MA) (yellow), 2,6-dihydroxynaphthalene (light blue), 1,3-dihydroxynaphthalene (1,3-DHN) (purple), 1-naphthol (brown), 2-naphthol (pink), uracil (green) and poly1-HN (blue), scaled with respect to Quartier's peak at 1643 cm<sup>-1</sup> and offset for clarity. **b**, Corresponding co-located fluorescence spectra, normalized on maximum and offset for clarity. The dashed line marks the onset of the spectral region beyond SHERLOC's detection range.

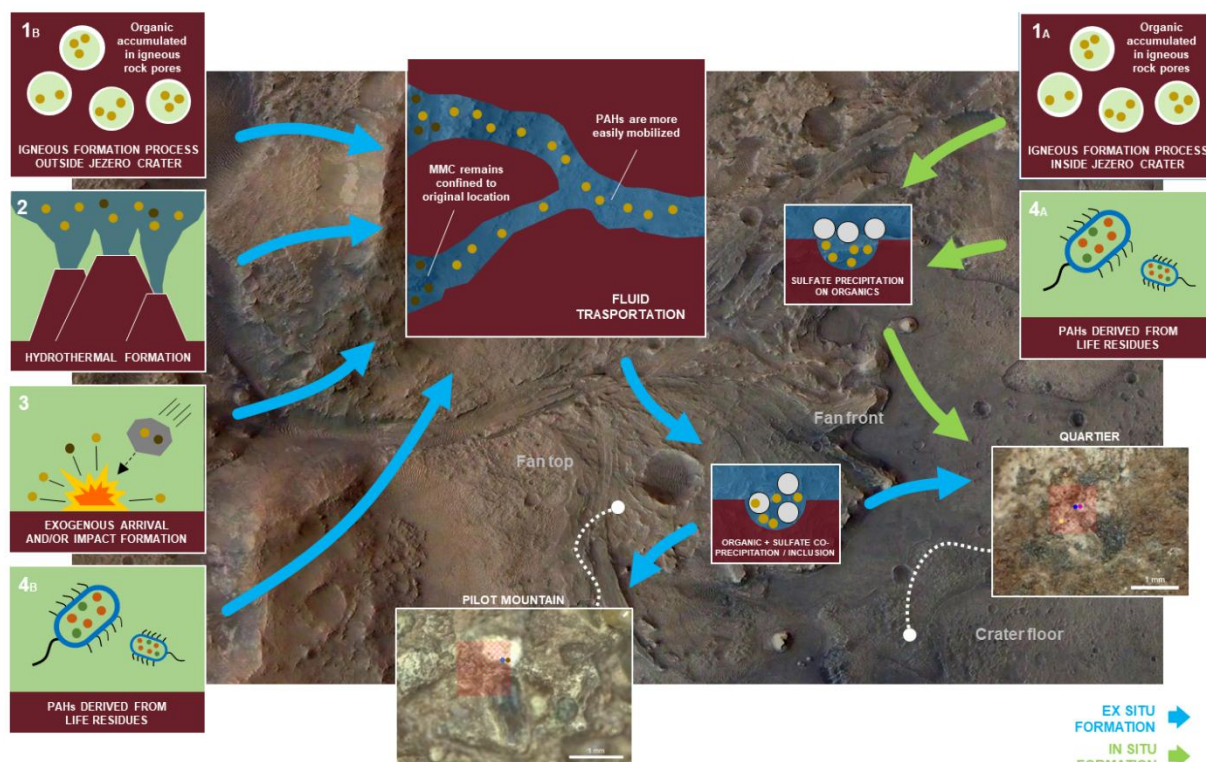


**Fig. 5. Sketch of potential mechanisms for the presence of PAHs in sulfates in Quartier and Pilot Mountain.** Scenario 1A describes an *in situ* igneous process for PAH formation from magmatic gases trapped in pores of igneous rocks of Jezero crater, followed by preservation by sulfates precipitated as consequence of aqueous alteration, which might be consistent with Quartier observations. Scenario 1B describes an *ex situ* igneous formation of PAHs, occurred outside Jezero crater, followed by fluid transportation of PAHs towards Jezero crater, where PAHs might have been co-precipitated with sulfates or trapped and preserved within sulfate cement crystals. This scenario might be consistent with both Quartier and Pilot Mountain observations, and the selective accumulation of PAHs in these rocks instead of macromolecular carbon (MMC) due to its lower mobility in fluid phases. Scenario 2 describes a potential hydrothermal formation of PAHs and transportation by hydrothermal groundwaters that might have been related to regional hydrothermalism associated with Syrtis Major volcanism. Scenario 3 describes a potential exogeneous delivery of PAHs or production during shock impact processes. Scenario 4 describes a potential biotic origin of the PAHs as chemical weathering products of ancient biotic compounds. The locations of the Quartier and Pilot Mountain targets in Jezero crater are shown on an image taken by the High Resolution Stereo Camera on ESA's Mars Express orbiter (Credits: ESA/DLR/FU-Berlin/NASA/JPL-Caltech). Green arrows indicate *in situ* formation mechanisms, while blue arrows indicate *ex situ* formation mechanisms.

## References

1. Farley, K. A. *et al.* Mars 2020 Mission Overview. *Space Sci Rev* **216**, 1–41 (2020).
2. Sharma, S. *et al.* Diverse organic-mineral associations in Jezero crater, Mars. *Nature* **619**, 724–732 (2023).
3. Siebach, K. L. *et al.* PIXL Analyses of Sedimentary Rocks in the Mars 2020 Perseverance Upper Fan Campaign in Jezero Crater. in *55th Lunar and Planetary Science Conference abstr. no. 2365 (Lunar and Planetary Institute, 2024)* vol. 3040.
4. Treiman, A. H. *et al.* Mount Meeker: A Boulder of Aluminous Melt Rock in Jezero Crater, Mars. in *55th Lunar and Planetary Science Conference abstr. no. 1283 (Lunar and Planetary Institute, 2024)* vol. 3040.
5. Siljeström, S. *et al.* Evidence of Sulfate-Rich Fluid Alteration in Jezero Crater Floor, Mars. *J Geophys Res Planets* **129**, e2023JE007989 (2024).
6. Phua, Y. Y. *et al.* Characterizing Hydrated Sulfates and Altered Phases in Jezero Crater Fan and Floor Geologic Units With SHERLOC on Mars 2020. *J Geophys Res Planets* **129**, e2023JE008251 (2024).
7. Fornaro, T. *et al.* Infrared Spectral Investigations of UV Irradiated Nucleobases Adsorbed on Mineral Surfaces. *Icarus* **226**, 1068–1085 (2013).
8. Fornaro, T. *et al.* UV irradiation of biomarkers adsorbed on minerals under Martian-like conditions: Hints for life detection on Mars. *Icarus* **313**, 38–60 (2018).
9. Fornaro, T. *et al.* Binding of Nucleic Acid Components to the Serpentinite-hosted Hydrothermal Mineral Brucite. *Astrobiology* **18**, 989–1007 (2018).
10. Fornaro, T. *et al.* UV Irradiation and Near Infrared Characterization of Laboratory Mars Soil Analog Samples. *Frontiers in Astronomy and Space Sciences* **7**, 539289 (2020).
11. Razzell Hollis, J. *et al.* A Deep Ultraviolet Raman and Fluorescence Spectral Library of 51 Organic Compounds for the SHERLOC Instrument Onboard Mars 2020. *Astrobiology* **23**, 1–23 (2023).
12. Haney, N. C. *et al.* Inorganic interpretation (anhydrite:Ce<sup>3+</sup>) of the 305 and 325 nm luminescence doublet detected by the SHERLOC instrument onboard the Mars2020 Perseverance rover. in *55th Lunar and Planetary Science Conference abstr. no. 2372 (Lunar and Planetary Institute, 2024)*.
13. Sharma, S. *et al.* Luminescence of cerium(III) in natural sulfates: an examination of analog minerals on Earth and implications for cerium presence on Mars. in *55th Lunar and Planetary Science Conference abstr. no. 2006 (Lunar and Planetary Institute, 2024)*.
14. Steele, A. *et al.* A reduced organic carbon component in martian basalts. *Science* **337**, 212–215 (2012).
15. Steele, A. *et al.* Organic synthesis associated with serpentinization and carbonation on early Mars. *Science* **375**, 172–177 (2022).
16. McKay, D. S. *et al.* Search for past life on Mars: possible relic biogenic activity in martian meteorite ALH84001. *Science* **273**, 924–930 (1996).

17. Steele, A. *et al.* Graphite in the martian meteorite Allan Hills 84001. *American Mineralogist* **97**, 1256–1259 (2012).
18. Zolotov, M. Y. & Shock, E. L. An abiotic origin for hydrocarbons in the Allan Hills 84001 martian meteorite through cooling of magmatic and impact-generated gases. *Meteorit Planet Sci* **35**, 629–638 (2000).
19. Zolotov, M. Y. & Shock, E. L. A thermodynamic assessment of the potential synthesis of condensed hydrocarbons during cooling and dilution of volcanic gases. *J Geophys Res Solid Earth* **105**, 539–559 (2000).
20. Tingle, T. N. & Hochella, M. F. Formation of reduced carbonaceous matter in basalts and xenoliths: Reaction of C-O-H gases on olivine crack surfaces. *Geochim Cosmochim Acta* **57**, 3245–3249 (1993).
21. Tingle, T. N., Hochella, M. F., Becker, C. H. & Malhotra, R. Organic compounds on crack surfaces in olivine from San Carlos, Arizona and Hualalai Volcano, Hawaii. *Geochim Cosmochim Acta* **54**, 477–485 (1990).
22. Andreani, M. *et al.* The rocky road to organics needs drying. *Nature Communications* **14**(1), 347 (2023).
23. Steele, A. *et al.* Organic synthesis on Mars by electrochemical reduction of CO<sub>2</sub>. *Sci Adv* **4**, eaat5118 (2018).
24. Aubrey, A. *et al.* Sulfate minerals and organic compounds on Mars. *Geology* **34**, 357–360 (2006).
25. Sephton, M. A., Tan, J. S. W., Watson, J. S., Hickman-Lewis, K. & Madariaga, J. M. Organic geochemistry of in situ thermal-based analyses on Mars: the importance and influence of minerals. *J Geol Soc London* **180**, (2023).
26. Alberini, A. *et al.* Investigating the stability of aromatic carboxylic acids in hydrated magnesium sulfate under UV irradiation to assist detection of organics on Mars. *Scientific Reports* **14**, 15945 (2024).
27. Karmanocky, F. J. & Benison, K. C. A fluid inclusion record of magmatic/hydrothermal pulses in acid Salar Ignorado gypsum, northern Chile. *Geofluids* **16**, 490–506 (2016).
28. Mimura, K. Synthesis of polycyclic aromatic hydrocarbons from benzene by impact shock: Its reaction mechanism and cosmochemical significance. *Geochim Cosmochim Acta* **59**, 579–591 (1995).
29. Liu, Y. *et al.* An olivine cumulate outcrop on the floor of Jezero crater, Mars. *Science* **377**, 1513–1519 (2022).
30. Stack, K. M. *et al.* Sedimentology and Stratigraphy of the Shenandoah Formation, Western Fan, Jezero Crater, Mars. *J Geophys Res Planets* **129**, e2023JE008187 (2024).
31. Canfield, D. E. & Raiswell, R. The evolution of the sulfur cycle. *Am J Sci* **299**, 697–723 (1999).
32. Jaramillo, E. A., Royle, S. H., Claire, M. W., Kounaves, S. P. & Sephton, M. A. Indigenous Organic-Oxidized Fluid Interactions in the Tissint Mars Meteorite. *Geophys Res Lett* **46**, 3090–3098 (2019).
33. Eigenbrode, J. L. *et al.* Organic matter preserved in 3-billion-year-old mudstones at Gale crater, Mars. *Science* **360**, 1096–1101 (2018).
34. Corpolongo, A. *et al.* SHERLOC Raman Mineral Class Detections of the Mars 2020 Crater Floor Campaign. *J Geophys Res Planets* **128**, e2022JE007455 (2023).

35. Shkolyar, S. *et al.* Detecting Ce<sup>3+</sup> as a biosignature mimicker using UV time-resolved laser-induced fluorescence and Raman spectroscopy: Implications for planetary missions. *Icarus* **354**, 114093 (2021).
36. Scheller, E. L. *et al.* Inorganic interpretation of luminescent materials encountered by the Perseverance rover on Mars. *Sci Adv* **10**, 8241 (2024).
37. Williams, A. *et al.* Diverse Organic Molecules on Mars Revealed by the first SAM TMAH Experiment. in *55th Lunar and Planetary Science Conference abstr. no. 1999 (Lunar and Planetary Institute, 2024)*.
38. Remusat, L., Derenne, S., Robert, F. & Knicker, H. New pyrolytic and spectroscopic data on Orgueil and Murchison insoluble organic matter: A different origin than soluble? *Geochim Cosmochim Acta* **69**, 3919–3932 (2005).
39. Jensen, T. R., Christensen, A. N., Olesen, M. & Cerenius, Y. Formation and transformation of five different phases in the CaSO<sub>4</sub>-H<sub>2</sub>O System: Crystal structure of the subhydrate β-CaSO<sub>4</sub>·0.5H<sub>2</sub>O and soluble anhydrite CaSO<sub>4</sub>. *Chemistry of Materials* **20**, 2124–2132 (2008).
40. Clark, J. V. *et al.* Combined Thermal and Evolved Gas Analysis, X-Ray Diffraction, Vis-NIR, X-Ray Fluorescence, and DUV Raman Spectroscopy of Synthetic Amorphous Magnesium Sulfates and Starkeyite: Implications for the Detection of Mg Sulfates by the Sample Analysis at Mars Instrument in Gale Crater, Mars. in *54th Lunar and Planetary Science Conference abstr. no. 2441 (Lunar and Planetary Institute, 2023)* vol. 2806.
41. Cecchini, M. M., Reale, S., Manini, P., d’Ischia, M. & De Angelis, F. Modeling Fungal Melanin Buildup: Biomimetic Polymerization of 1,8-Dihydroxynaphthalene Mapped by Mass Spectrometry. *Chemistry – A European Journal* **23**, 8092–8098 (2017).
42. Manini, P. *et al.* “Blackness” is an index of redox complexity in melanin polymers. *Polym Chem* **11**, 5005–5010 (2020).
43. Keheyani, Y. & ten Kate, I. L. Radiolytic Studies of Naphthalene in the Presence of Water. *Origins of Life and Evolution of Biospheres* **42**, 179–186 (2012).
44. Kebukawa, Y., David Kilcoyne, A. L. & Cody, G. D. Exploring the Potential Formation of Organic Solids in Chondrites and Comets through Polymerization of Interstellar Formaldehyde. *Astrophys J* **771**, 19 (2013).
45. Fornaro, T. *et al.* Evidence for polycyclic aromatic hydrocarbons detected in sulfates by Perseverance’s deep UV Raman spectrometer at Jezero crater, Mars [Data set]. *Open Data Repository* (2024) doi:<https://doi.org/10.48484/SS9A-K041>.
46. Uckert, K. Loupe (Version V5.1.5). *Zenodo* <https://zenodo.org/records/7062998> (2022) doi:10.5281/ZENODO.7062998.
47. Razzell Hollis, J. *et al.* A deep-ultraviolet Raman and Fluorescence spectral library of 62 minerals for the SHERLOC instrument onboard Mars 2020. *Planet Space Sci* **209**, 105356 (2021).
48. Jakubek, R. S. *et al.* Calibration of Raman Bandwidths on the Scanning Habitable Environments with Raman and Luminescence for Organics and Chemicals (SHERLOC) Deep Ultraviolet Raman and Fluorescence Instrument Aboard the Perseverance Rover. *Appl Spectrosc* **78**(9), 993-1008 (2024).
49. Bhartia, R. *et al.* Perseverance’s Scanning Habitable Environments with Raman and Luminescence for Organics and Chemicals (SHERLOC) Investigation. *Space Sci Rev* **217**, 58 (2021).
50. Sharma, S. *et al.* Multi-instrument Image Correlation for In Situ Planetary Science on Mars 2020. *IEEE Aerospace Conference Proceedings* (2024) doi:10.1109/AERO58975.2024.10521366.

51. Allwood, A. C. *et al.* PIXL: Planetary Instrument for X-Ray Lithochemistry. *Space Sci Rev* **216**, 1–132 (2020).
52. Orenstein, B. J. *et al.* A statistical approach to removing diffraction from X-ray fluorescence spectra. *Spectrochim Acta Part B At Spectrosc* **200**, 106603 (2023).
53. Tice, M. M. *et al.* Alteration history of Séítah formation rocks inferred by PIXL x-ray fluorescence, x-ray diffraction, and multispectral imaging on Mars. *Sci Adv* **8**, (2022).
54. Heirwegh, C. M., Elam, W. T., O’Neil, L. P., Sinclair, K. P. & Das, A. The focused beam X-ray fluorescence elemental quantification software package PIQUANT. *Spectrochim Acta Part B At Spectrosc* **196**, 106520 (2022).
55. Tice, M. M. *et al.* PIXL on Perseverance as a Complete X-ray Spectroscopic Instrument: Analyzing X-ray Fluorescence, Scattering, and Diffraction in Martian Rocks. in *54th Lunar and Planetary Science Conference abstr. no. 2659 (Lunar and Planetary Institute, 2023)* vol. 2806.
56. Alvarado-Jiménez, D. & Tasinato, N. In silico modelling of radiative efficiencies of anthropogenic greenhouse gases. *Atmos Environ* **338**, 120839 (2024).
57. Santra, G., Sylvetsky, N. & Martin, J. M. L. Minimally Empirical Double-Hybrid Functionals Trained against the GMTKN55 Database: RevDSD-PBEP86-D4, revDOD-PBE-D4, and DOD-SCAN-D4. *Journal of Physical Chemistry A* **123**, 5129–5143 (2019).
58. Papajak, E., Zheng, J., Xu, X., Leverentz, H. R. & Truhlar, D. G. Perspectives on basis sets beautiful: Seasonal plantings of diffuse basis functions. *J Chem Theory Comput* **7**, 3027–3034 (2011).
59. Zhao, Y. & Truhlar, D. G. Design of density functionals that are broadly accurate for thermochemistry, thermochemical kinetics, and nonbonded interactions. *Journal of Physical Chemistry A* **109**, 5656–5667 (2005).
60. Becke, A. D. Density-functional Thermochemistry. III. The Role of Exact Exchange. *J Chem Phys* **98**, 5648–5652 (1993).
61. Grimme, S., Antony, J., Ehrlich, S. & Krieg, H. A consistent and accurate ab initio parametrization of density functional dispersion correction (DFT-D) for the 94 elements H-Pu. *J. Chem. Phys.* **132**, 154104 (2010).
62. Grimme, S., Ehrlich, S. & Goerigk, L. Effect of the damping function in dispersion corrected density functional theory. *J Comput Chem* **32**, 1456–1465 (2011).
63. Papoušek, D. & Aliev, M. R. *Molecular Vibrational-Rotational Spectra: Theory and Applications of High Resolution Infrared, Microwave, and Raman Spectroscopy of Polyatomic Molecules.* (Amsterdam; New York: Elsevier Scientific Pub. Co., 1982).
64. Puzzarini, C., Bloino, J., Tasinato, N. & Barone, V. Accuracy and Interpretability: The Devil and the Holy Grail. New Routes across Old Boundaries in Computational Spectroscopy. *Chem Rev* **119**, 8131–8191 (2019).
65. Bloino, J., Biczysko, M. & Barone, V. General Perturbative Approach for Spectroscopy, Thermodynamics, and Kinetics: Methodological Background and Benchmark Studies. *J Chem Theory Comput* **8**, 1015–1036 (2012).
66. Ceselin, G., Salta, Z., Bloino, J., Tasinato, N. & Barone, V. Accurate Quantum Chemical Spectroscopic Characterization of Glycolic Acid: A Route Toward its Astrophysical Detection. *Journal of Physical Chemistry A* **126**, 2373–2387 (2022).

**Correspondence and requests for materials should be addressed to T. Fornaro.**

